Ratio-based sensing of two transcription factors regulates the transit to differentiation

Sebastian M. Bernasek[1]*, Jean-François Boisclair Lachance[2]*, Nicolás Peláez[1,3,4]*, Suzy SJ Hur[2], Rachael Bakker[3], Heliodoro Tejedor Navarro[1], Nicelio Sanchez-Luege[2], Luis A. N. Amaral[1,5,6,7], Neda Bagheri[1,6,7,8], Ilaria Rebay[2†], and Richard W. Carthew[3,7,9†]

[1]Department of Chemical and Biological Engineering, Northwestern University, Evanston, IL
[2]Ben May Department for Cancer Research, University of Chicago, Chicago, IL
[3]Department of Molecular Biosciences, Northwestern University, Evanston, IL
[4]Division of Biology and Biological Engineering, California Institute of Technology, Pasadena, CA
[5]Department of Physics and Astronomy, Northwestern University, Evanston, IL
[6]Northwestern Institute on Complex Systems, Northwestern University, Evanston, IL
[7]NSF-Simons Center for Quantitative Biology, Northwestern University, Evanston, IL
[8]Chemistry of Life Processes, Northwestern University, Evanston, IL
[9]Department of Biochemistry and Molecular Genetics, Northwestern University, Evanston, IL

* These authors made equal contributions

† Corresponding authors (irebay@uchicago.edu; r-carthew@northwestern.edu)

ABSTRACT

Cell state transitions are usually thought to be triggered by changes in the absolute concentrations of relevant transcription factors. In the *Drosophila* eye, the transcription factor Yan maintains cells in a progenitor state by repressing gene expression, while the Pointed transcription factor activates gene expression programs that promote photoreceptor specification. In this study we investigate how retinal cell state transitions are resolved by quantifying the expression dynamics of Yan and Pointed proteins. Despite extensive cell-to-cell variation in absolute concentrations of Yan and Pointed, progenitor cells maintain a relatively constant ratio of Pointed-to-Yan protein. A sustained change in the Pointed-to-Yan ratio accompanies the transition to photoreceptor fates. Genetic perturbations that disrupt the ratio produce photoreceptor specification defects, suggesting that transitions depend upon a sustained change in the ratio. A model based on the statistical physics of protein-DNA binding illustrates how ratiometric sensing could produce the changes in gene expression that underlie these cell state transitions. We propose that ratiometric control mechanisms facilitate regulation of developmental transitions by multiple transcription factors, and thereby make the transitions robust to fluctuations in absolute protein levels.

INTRODUCTION

Organismal development proceeds through a sequence of transitions that yield increasingly specific cellular states. Conceptually, cell state transitions are often modeled as dynamical systems with bistability, with transitions viewed as irreversible switches between two stable but molecularly distinct cell states. Developmental transitions must be both accurate and robust so that the correct types and numbers of cells needed to pattern each tissue are generated reliably at the right time and place.

Transcription factors play central roles in defining each state and in orchestrating the transition between them. Genetic studies of numerous cell state transitions in metazoans have identified the relevant transcription factors, organized them into networks and defined the activating or repressive inputs that promote or prevent the transition. Network topology, namely the regulatory relationships between the transcription factors that define the network, can produce systems with mono-, bi- or multi-stability. For example, a simple mutually repressive circuit between two transcription factors can produce switch-like transitions between two stable states (Edgar et al., 1989; Gardner et al., 2000; Graham et al., 2010; Jacob and Monod, 1961). Networks with more elaborate circuits of positive and negative feedback render such state transitions more robust and irreversible (Melen et al., 2005; Schröter et al., 2015; Yao et al., 2008). While these network views provide useful abstract frameworks to define the states and the transitions between them, achieving quantitative understanding of how transcription factor expression and activity levels are modulated before, during and after a transition and how these dynamics contribute to the specificity, robustness and stability of cell state transitions remains challenging.

There are potentially two different strategies for how changes in transcription factor abundance might orchestrate specific transitions. First, studies of several networks, for example those regulating hematopoietic cell fate specification and the embryonic stem cell pluripotency-differentiation transition, have shown that transcription factors can provide ultrasensitive regulation such that small changes in their absolute concentrations trigger distinct differentiative transitions (Gillespie et al., 2020; Kopp et al., 2008; Laslo et al., 2006; Niwa et al., 2000). A second possible strategy might involve the response being sensitive to fold-change in transcription factor concentrations. This hypothesis is inspired by the finding that cells appear capable of sensing relative levels of signaling molecules. For example, in cultured cell models, changes in gene expression downstream of the TGF-β or Wnt signaling pathways occur in response to fold-changes rather than to absolute levels of the transcriptional effectors(Frick et al., 2017; Goentoro and Kirschner, 2009). Whether cells in a developing multicellular animal can similarly gauge and interpret relative concentrations of different transcription factors to execute state transitions is not known.

54 In this study we investigate how state transitions in the *Drosophila* eye imaginal disc are resolved
55 from a starting point of concurrent expression of two ETS-domain transcription factors, the activator
56 Pointed (Pnt) and the repressor Yan (also known as Anterior open, Aop). These transcriptional effectors
57 operate downstream of the receptor tyrosine kinase (RTK) – MAP kinase (MAPK) pathway in *Drosophila*,
58 providing essential regulation to numerous cell fate transitions (O'Neill et al., 1994; Vivekanand and
59 Rebay, 2006). Across a variety of developmental contexts, loss of *yan* results in too many progenitors
60 transiting to a particular fate whereas loss of *pnt* prevents the transition, leading to loss of that fate
61 (Brunner et al., 1994; Flores et al., 2000; Gabay et al., 1996; Halfon et al., 2000; O'Neill et al., 1994; Xu
62 et al., 2000). Conversely, excess Yan repressive activity can prevent transitions while excess Pnt activity
63 can trigger ectopic fate specification (Brunner et al., 1994; Lachance et al., 2018; Rebay and Rubin,
64 1995; Shwartz et al., 2013; Wu et al., 2020).

65 These opposing phenotypes, together with elucidation of the extensive feedback circuitry that
66 defines the Pnt-Yan network, inspired development of a bistable model for cell fate specification in which
67 the progenitor state is defined by high absolute Yan concentrations and the differentiated state is defined
68 by high absolute Pnt concentrations (Brunner et al., 1994; Gabay et al., 1996; Graham et al., 2010; Li et
69 al., 2009; Melen et al., 2005; Qiao et al., 2004b; Tootle et al., 2003; Vivekanand et al., 2004; Yamada et
70 al., 2003). The transition between the two states occurs when RTK-MAPK signaling triggers concomitant
71 downregulation of Yan activity and expression, and upregulation of Pnt activity and expression.

72 While this model readily explains transitions where mutually exclusive Pnt and Yan expression
73 define distinct cell states (Gabay et al., 1996; Melen et al., 2005), other well-studied transitions, such as
74 those occurring in the embryonic mesoderm and in the eye imaginal disc, begin with extensive Pnt and
75 Yan co-expression in the progenitor pool (Lachance et al., 2014). Qualitative comparison of Pnt and Yan
76 protein expression in the developing eye suggest that Pnt and Yan levels also decay on comparable
77 timescales in transitioning cells (Lachance et al., 2014). Reconciling these transitions with the bistable
78 model has proven difficult because the quantitative features that define them are not well-characterized.

79 In an earlier study, we developed a quantitative approach to study Yan dynamics in the
80 developing eye disc (Peláez et al., 2015). We found that Yan exhibits monostable patterns of expression
81 in both progenitor cells and differentiating photoreceptors, and that cell state transitions occur
82 independent of absolute Yan concentration. These results motivated us to consider whether the
83 molecular events that drive and accompany cell state transitions might be more clearly reflected by the
84 collective Pnt and Yan expression dynamics than by the expression of either Yan or Pnt alone.

Here we report the results of quantifying Pnt and Yan expression in thousands of individual eye cells. We find that cell state transitions are marked by changes in the relative abundance of these two transcription factors, rather than by their absolute concentrations. Multipotent progenitor cells maintain an approximately constant ratio of Pnt-to-Yan protein over time despite extensive cell-to-cell variation in absolute concentrations. Cells that transition to photoreceptor fates rapidly increase their Pnt-to-Yan ratio at the time of specification. As differentiation proceeds, the ratio decays but remains stably elevated above the progenitor ratio. Manipulations of *pnt* or *yan* gene dose showed that the Pnt-to-Yan protein ratio is remarkably robust to changes in absolute transcription factor concentration, revealing the existence of a ratio control strategy that may buffer the system against variable abundance of either transcription factor. Genetic perturbations designed to circumvent this compensatory mechanism caused abnormally high or low Pnt-to-Yan ratios, resulting in respective gain or loss of cell state transitions and defects in retinal patterning. We propose that developing eye cells rely on a ratiometric sensing mechanism in which a sustained increase in Pnt-to-Yan ratio initiates and accompanies differentiative transitions.

RESULTS

Cell state transitions coincide with two pulses of increased Pnt protein levels

The stereotyped, repetitive events that pattern the developing *Drosophila* compound eye provide a tractable context in which to quantify and compare transcription factor expression dynamics at single cell resolution during cell state transitions. Photoreceptor cell fate specification is initiated and coordinated across hundreds of identical ommatidial units by passage of the morphogenetic furrow (MF) (Figure 1A; Voas and Rebay, 2004; Wolff and Ready, 1993). As the MF traverses the eye disc from posterior to anterior over about two days of late larval and early pupal development, progenitor cells immediately anterior to the MF turn on expression of the transcription factor Atonal. Refinement of Atonal expression defines a column of future ommatidial units by specifying individual R8-type photoreceptors in a periodic pattern immediately posterior and parallel to the MF (Jarman et al., 1994; Zhang et al., 2006). Each R8 cell secretes the protein Spitz, which locally binds and activates Epidermal Growth Factor Receptor (EGFR) in neighboring progenitor cells. Signals transduced via the Ras-MAPK cascade and interpreted by Pnt and Yan, trigger the sequential recruitment of the R2/R5, R3/R4, R1/R6, and R7 photoreceptor types to each ommatidium (Figure 1B; Freeman, 1996; Voas and Rebay, 2004). Many multipotent progenitors remain after all R cell fates have been specified and adopt other fates at later stages of eye development, with any final surplus eliminated by apoptosis (Wolff and Ready, 1991).

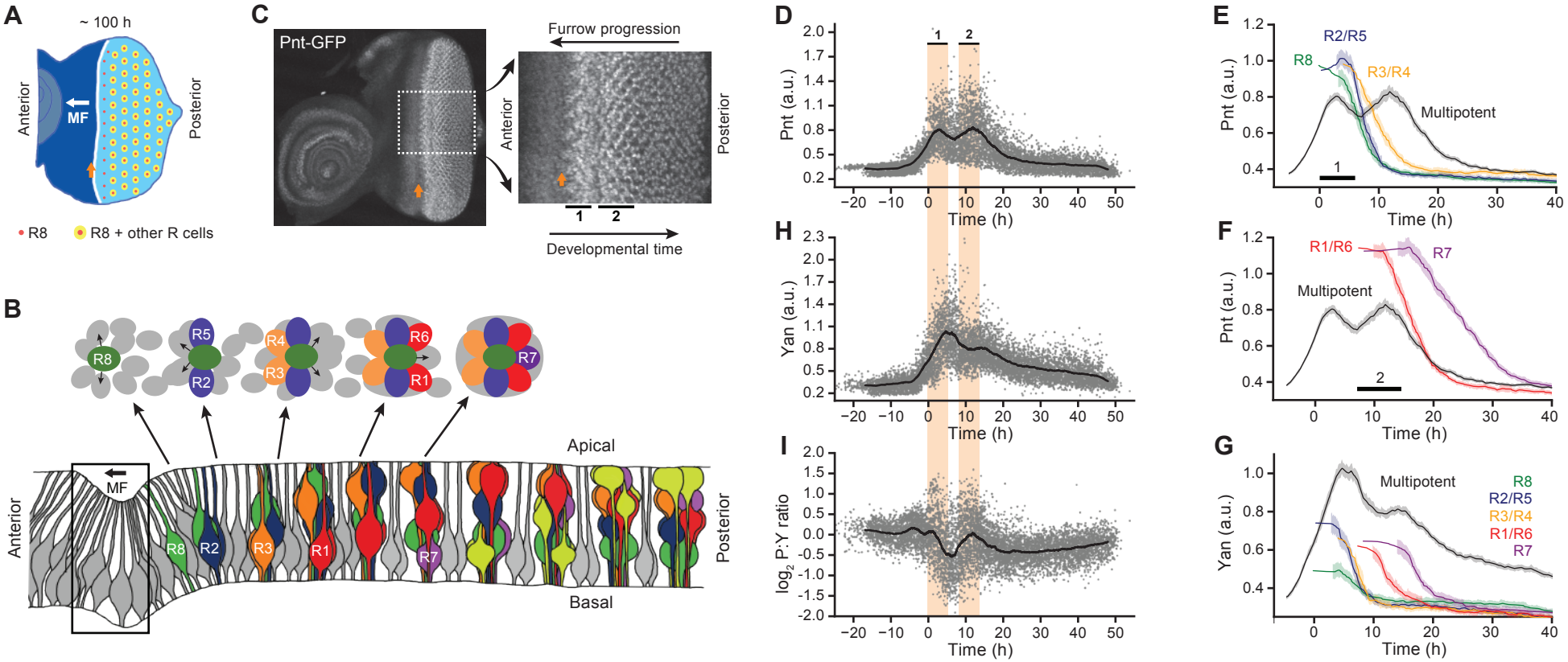

Figure 1: Dynamics of Pnt and Yan expression during eye development. See figure supplements 1-3

(A) Schematic of an eye imaginal disc dissected from an animal ~100 hours post fertilization (25°C). Differentiation is initiated by passage of the morphogenetic furrow (MF), which moves across the eye epithelium from posterior to anterior (white arrow). Anterior progenitors (dark blue) proliferate asynchronously, while progenitor cells posterior to the furrow (light blue) arrest in G1 and then undergo a stereotyped sequence of state transitions. Specification of regularly spaced R8 cells (red dots) marks the start of ommatidial assembly and is followed by recruitment of additional R cell types (yellow dots). Adapted from Peláez et al. (2015).

(B) Top, cartoon of an apical view of the sequential differentiation of eight R cell types from multipotent progenitor cells (grey) and their relative positions within a single ommatidium. Arrows denote signals transmitted from the R8 to nearby cells. Bottom, a cross-section view through an eye disc, showing the epithelial constriction that marks the MF (boxed region) and then the relative nuclear positions of progenitors (grey) and specified R cells (various colors). Together, the stereotyped features depicted in this schematic enable unambiguous identification of each cell type as ommatidial assembly proceeds. Adapted from Peláez et al. (2015).

(C) Maximum intensity projection of Pnt-GFP fluorescence in an imaginal disc fixed ~100 h after fertilization. Right panel corresponds to the region enclosed by dashed white lines in the left panel. Morphogenetic furrow (orange arrow) precedes the first and second stripes of strong Pnt-GFP expression (black lines, labeled 1 and 2).

(D) Pnt-GFP abundance in progenitor cells. Grey points are individual nuclei, solid line is the smoothed moving average. Orange shading indicates the two regions of peak Pnt-GFP expression.

(E,F) R cell recruitment from the **(E)** first and **(F)** second peaks of Pnt-GFP expression in progenitors (grey). Solid lines and shaded regions denote moving averages and their 95% confidence intervals.

(G) Patterns of R cell recruitment relative to peak of Yan expression in progenitors (grey). Solid lines and shaded regions denote moving averages and their 95% confidence intervals. See also Pelaez et al., 2015.

(H, I) Measured **(H)** Yan abundance and **(I)** log2-transformed Pnt-to-Yan ratios in progenitor cells. Grey points are individual cells, solid line is a smoothed moving average.

117 Because the MF moves across the eye field with approximately constant velocity, initiating a new
118 column of R8 cells every two hours (Basler and Hafen, 1989; Campos-Ortega and Hofbauer, 1977) the
119 distance between the MF and any cell posterior to it is linearly proportional to the time elapsed since the
120 MF passed. This allows each cell's position along the anterior-posterior axis of the eye disc to be
121 mapped to a point in developmental time. Further, the highly stereotyped morphogenesis accompanying
122 each cell fate transition allows unambiguous identification of progenitor and differentiated photoreceptor
123 (R1-R8) states using only nuclear morphology and apical-basal position (Figure 1B; Peláez et al., 2015;
124 Tomlinson and Ready, 1987; Wolff and Ready, 1993). Using these same features, newly specified or
125 "young" R cells can be readily distinguished from both the concurrent progenitors and the "older" mature
126 R cells (Ready et al., 1976; Tomlinson, 1985). Cross-referencing with cell-specific markers has confirmed
127 we can make cell state assigments with >95% accuracy (Peláez et al., 2015). Although our approach
128 cannot measure the developmental progression of an individual cell, it provides a dynamic view of
129 thousands of cells across a developing eye. From this macroscopic view of dynamics, average cell
130 behaviors can be reconstructed and modeled.

131 Using this system together with a fully-functional genomic transgene in which all *pnt* isoforms are
132 C-terminally tagged with GFP (Lachance et al., 2014; and Figure 1 - figure supplement 1A,B), we
133 quantified Pnt expression dynamics in thousands of individual retinal cells as they navigated the
134 progenitor to photoreceptor fate transition. Confocal z-stacks of fixed 100h eye imaginal discs from *pnt-*
135 *GFP;pnt*$^{-/-}$ animals were processed using our published automated nuclear segmentation pipeline (Peláez
136 et al., 2015) that measures average Pnt-GFP fluorescence levels and exact 3D positions for all nuclei
137 (Figure 1 – figure supplement 2). Normalizing Pnt-GFP fluorescence levels to levels of Histone-RFP or to
138 DAPI provided control over measurement noise and differences in nuclear volume (Figure 1 – figure
139 supplement 2).

140 Focusing first on the progenitor cells, we found Pnt-GFP exhibited a steady-state basal level of
141 expression in cells anterior to the MF, but then increased dramatically in cells immediately anterior to the
142 MF (Figure 1C,D). This increase culminated in two successive peaks where Pnt-GFP expression
143 reached maximal amplitude. Each of these two pulses results from unique combinations of three different
144 Pnt isoforms (Wu et al., 2020). After the second peak, Pnt-GFP decayed to a low basal level. These
145 patterns matched the previously described qualitative features of Pnt-GFP expression (Lachance et al.,
146 2014).

147 The two peaks of Pnt-GFP in progenitor cells coincided with the two periods when some
148 progenitors transition to R cell states (Figure 1E,F; Wu et al., 2020). Transitions to R8, R2/R5, and R3/R4

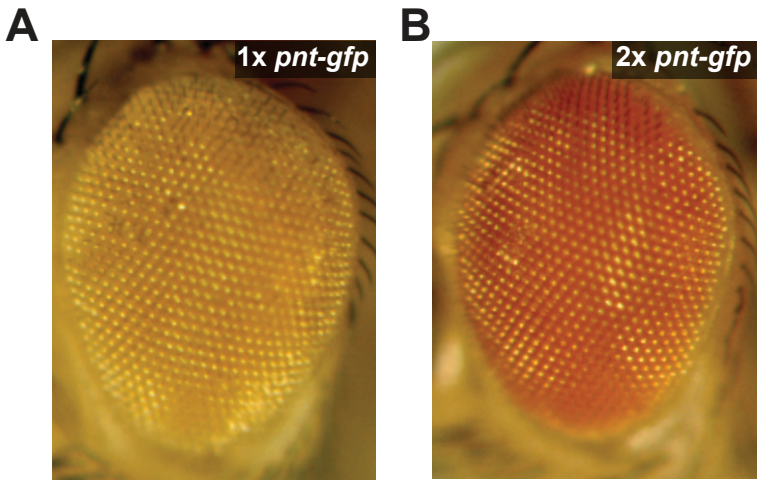

Figure 1 - figure supplement 1: Characterization of Pnt-GFP
Adult eyes of flies carrying **(A)** one or **(B)** two copies of the recombineered *pnt-gfp* transgene under a *pnt* null mutant background. Note the wildtype retina patterning under both rescue conditions.

!"# $%&')'*"#$%&'+$,,-&.&/0' (!"123%340&%"530"6/'6*'7/8 '
#$%&'"()(*"+,",&-(*"./00)-12"#4"+1("+0"354"6+".+7-(*"+,"'8("0(.+9: -1((0($" !"# $%&"!0/1*2(1("%1$(0" /" !"# "1%&&"9%'/1'"
:/.;20+%1$<"=+'("'8("6-&$')7("0('-1/"7/''(01-12" %1$(0":+'8"0(*.%(".+1$-'-+1*<"
!

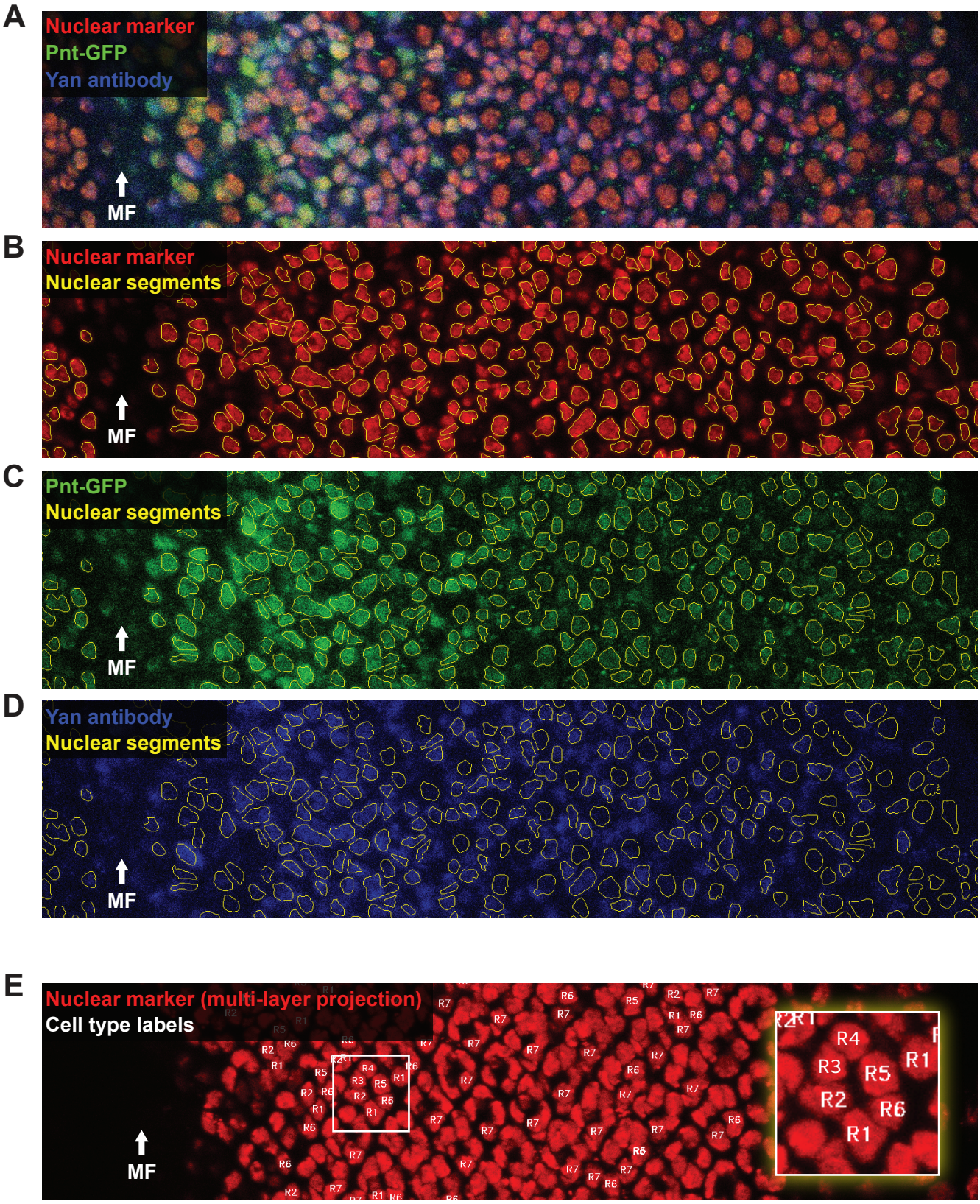

Figure 1 - figure supplement 2: Quantitative analysis pipeline
(A-D) Microscopy and segmentation of an example eye disc. **(A)** Partial cross-section of a confocal z-stack, with separate fluorescence channels for **(B)** Histone-RFP, **(C)** Pnt-GFP, and **(D)** Yan antibody. Yellow lines depict nuclear contours identified by FlyEye Silhouette.
(E) Manual annotation of R cell types without fate-specific markers. Image shows a maximum intensity projection of His-RFP fluorescence across four layers spanning early R cells. R cell types are readily distinguished by their morphological positions within each ommatidium.

149 states occurred during the first pulse, while transitions to R1/R6, and R7 states occurred during the
150 second. All cell state transitions coincided with a rapid increase in Pnt-GFP. The earliest identified R
151 cells, which we refer to as “young” R cells, were distinguished from the concurrent progenitors by 25-
152 50% higher Pnt-GFP levels on average. Immediately following the high expression peaks that marked
153 photoreceptor fate acquisition, Pnt-GFP expression decayed in all differentiating R cells, with all but R7
154 exhibiting faster decay kinetics than measured for the progenitor cells.

155 **An increase in Pnt-to-Yan ratio accompanies cell state transitions**

156 Overall, Pnt-GFP expression dynamics appeared remarkably similar to those we previously
157 reported for Yan (Figure 1 D-G; Peláez et al., 2015). At the population level, average levels of both
158 transcription factors increase in the progenitor pool as the MF passes, peak during R cell fate
159 specification, and then slowly decay. Similarly in transitioning R cells, instead of the stable high Pnt state
160 predicted by the traditional bistable model (Graham et al., 2010), both Pnt and Yan show rapid decay.
161 Because side-by-side population-wide views of Yan and Pnt-GFP expression dynamics in separate
162 samples does not allow simultaneous assessment of Yan and Pnt levels in individual cells, we measured
163 both Pnt-GFP and Yan in each nucleus using an anti-Yan monoclonal antibody. Although indirect
164 immunofluorescence risks non-linear amplification, we previously showed that Yan dynamics measured
165 with the antibody were almost identical to those measured directly with a fully-functional YFP tagged
166 version of Yan (Peláez et al., 2015), validating the approach.

167 Focusing first on the progenitor cells, we found that Pnt-GFP and Yan were induced at the same
168 time but peaked at different times (Figure 1D,H and Figure 1 - figure supplement 3A). Yan levels reached
169 a maximum amplitude between the two peaks of Pnt-GFP and then decayed back to a basal steady-
170 state level, interrupted by a transient plateau during the second pulse of Pnt-GFP. Despite their
171 alternating maxima, the overall induction and decay of Pnt-GFP and Yan were concurrent. Heat mapping
172 Yan levels onto each progenitor cell nucleus in the Pnt plot and vice versa emphasized the expression
173 heterogeneity within the two transition zones relative to the flanking regions (Figure 1 - figure supplement
174 3B,C).

175 The combination of similar population-level dynamics and regional heterogeneity prompted us to
176 consider whether the relative levels of Pnt and Yan might be coordinated in individual cells across the
177 progenitor population. To define these patterns more explicitly, we calculated the ratio of Pnt-to-Yan in
178 each progenitor cell. At the population level, the average Pnt-to-Yan ratio remained dynamically stable
179 about a constant value over time (Figure 1I). However, from 0 to 15 hours, there was considerable cell-
180 to-cell heterogeneity in the ratio. Coincident with the two peaks of Pnt-GFP, some cells had well above-

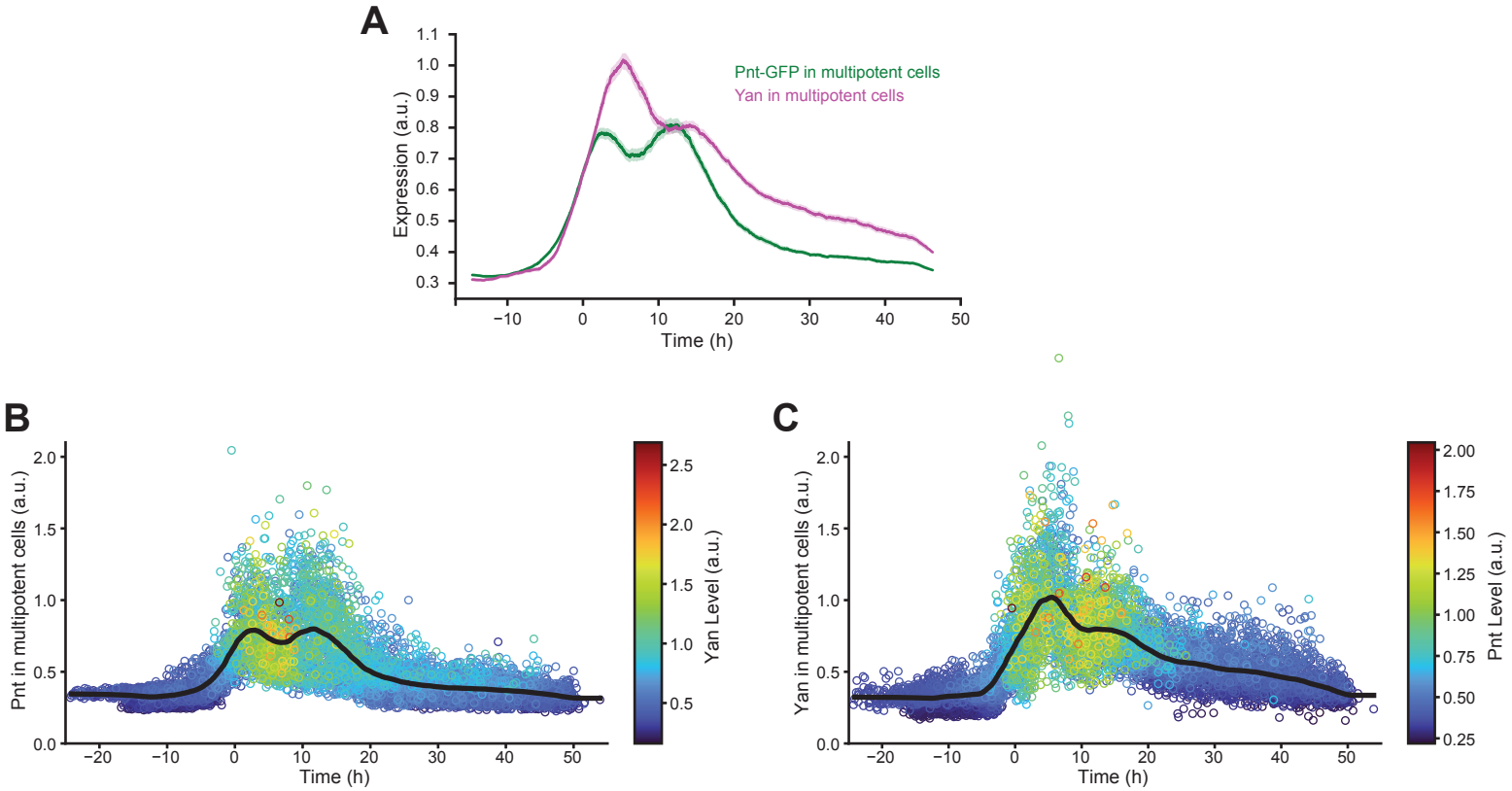

Figure 1 - figure supplement 3: Pnt-GFP and Yan expression in progenitor cells.
(A) Simultaneous Pnt-GFP (green) and Yan (magenta) expression dynamics in progenitor cells. Lines are smoothed moving averages across 500 sequential progenitors, shaded regions are bootstrapped 95% confidence intervals for the mean. Arrows indicate the times at which local maxima occur.
(B, C) Expression levels of **(B)** Pnt-GFP and **(C)** Yan in progenitor cells, color-coded in accordance with the expression level of the complementary transcription factor. In both panels, markers are arranged such that nuclei with higher levels of the complementary transcription factor are displayed in front. Lines are smoothed moving averages across 500 sequential progenitors.

181 average ratios, while in between the two Pnt-GFP peaks and coincident with the peak of Yan, many cells
182 had well below-average ratios. After the second pulse of Pnt-GFP expression, the remaining progenitor
183 cells, which remain multipotent and later differentiate into other cell types, acquired a slight bias towards
184 Yan.

185 The coincidence between the two positive spikes in the Pnt-to-Yan ratio and the two periods of
186 cell state transition suggested that dynamic changes in the ratio rather than in the absolute Yan or Pnt
187 levels might regulate the transit to differentiation. As a first test of this hypothesis, we quantified the
188 levels of Pnt-GFP and Yan in cells that had undergone R cell state transitions. We focused on R2/R5 and
189 R1/R6 cells, since they are representative of transitions of cells derived from progenitors in the first and
190 second Pnt-GFP peaks, respectively. As previously noted (Figure 1E,F), Pnt-GFP levels were elevated in
191 both sets of "young" R cells as soon as we could confidently distinguish them from the concurrent
192 progenitors (Figure 2A,B). In contrast, Yan levels were lower in these young R cells than in progenitor
193 cells of comparable age (Figure 2C,D). As a result, the average ratio of Pnt-to-Yan was elevated 1.5- to
194 2-fold in young R cells (Figure 2E,F). The elevation was more modest in young R2/R5 cells than in young
195 R1/R6 cells, but all increases were significant ($P<.001$, KS 2-sample test). The elevated ratio persisted
196 as differentiation proceeded and Yan and Pnt levels decayed, always remaining above that of the
197 progenitor pool. Analogous ratio trends were evident with the other R cell types (Figure 2G and Figure 2 -
198 figure supplement 1). We conclude that state transitions leading to the acquisition of photoreceptor fate
199 are defined by a sustained increase in the Pnt-to-Yan ratio relative to progenitor cells.

200 If high Pnt-to-Yan ratios initiate R cell fate transitions, then elevated ratios should precede the
201 onset of R cell states, resulting in overlap in ratios between young R cells and concurrent progenitors.
202 Alternatively, if Pnt-to-Yan ratios become elevated as a consequence of the transition, then the temporal
203 delay between onset of the fate and elevation of the ratio would result in less overlap. When we
204 compared the distribution of Pnt-to-Yan ratios in young R cells versus concurrent progenitor cells we
205 found extensive overlap between the two populations (Figure 2H,I). The high degree of overlap also
206 implies that if ratio elevation marks the onset of R cell state transitions, then some cells with high Pnt-to-
207 Yan ratios that we morphologically classified as progenitors at slightly earlier time points might actually
208 be in the very initial stages of transitioning to R cell fates. Many progenitors also adopted low Pnt-to-Yan
209 ratios that did not overlap with the early R cell population. Assuming these progenitors were not viable
210 candidates for effecting a state transition, then the extent of variation in the ratio among progenitors may
211 constrain competence for differentiation.

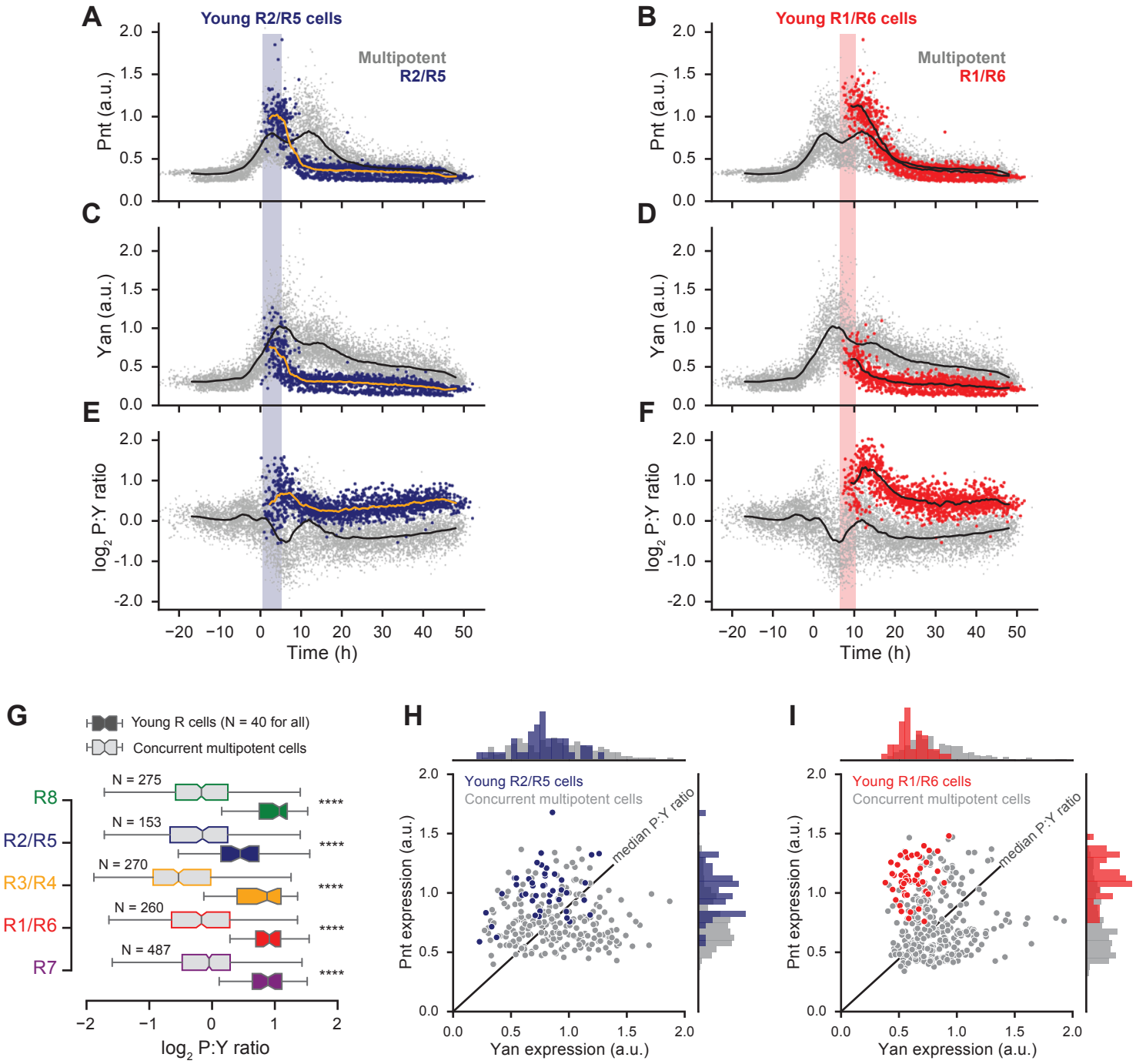

Figure 2: Pnt-to-Yan ratios differ between cellular states. See figure supplements 1 and 2.
(A-F) Measured **(A, B)** Pnt-GFP abundance, **(C, D)** Yan abundance, and **(E, F)** Pnt-GFP-to-Yan ratio dynamics in R2/R5 (blue) and R1/R6 (red) cells. Progenitor cells are grey. Solid lines are smoothed moving averages across 250 and 50 samples for progenitor and R cells, respectively. Shaded vertical stripes indicate time spanned by young R cells.
(G) Comparison of Pnt-to-Yan ratio levels between young R cells (color filled boxes) and their concurrent progenitors (grey filled boxes). Colors denote R cell types. For each R cell type, the ten earliest identifiable R cells in each disc were designated as young R cells. Progenitor cells that fall within the time window spanned by these young R cells were designated as concurrent progenitors. Asterisks indicate significant differences (P<.001, KS 2-sample test).
(H, I) Joint distributions of Pnt-GFP and Yan protein levels for young **(H)** R2/R5 and **(I)** R1/R6 cells. Progenitor cells concurrent with the corresponding young R cells are shown in grey. Black line denotes the median Pnt-to-Yan ratio among the progenitor cells shown.

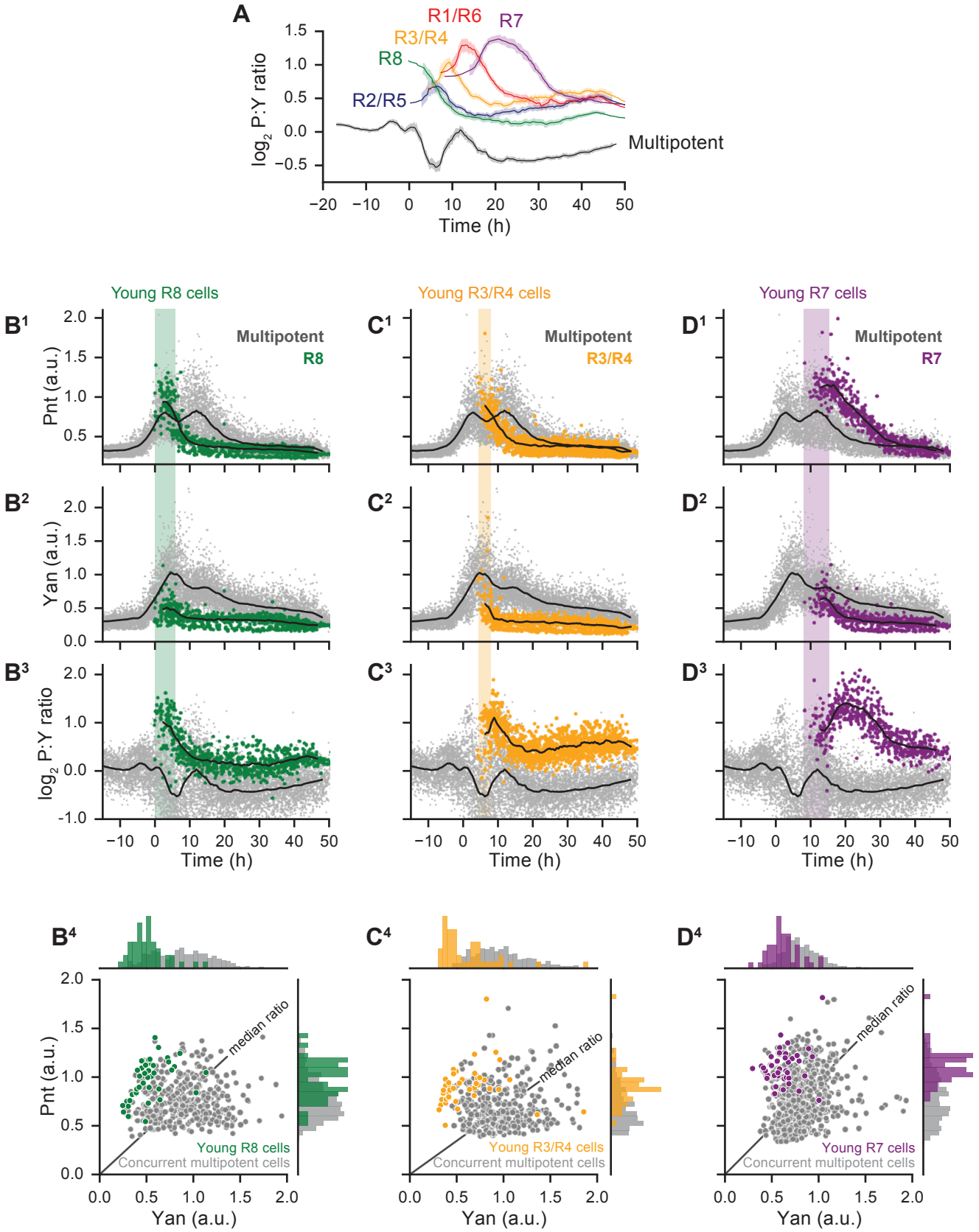

Figure 2 - figure supplement 1: Yan and Pnt expression dynamics.
(A) Measured Pnt-GFP-to-Yan ratio dynamics for all annotated cell types. Solid lines are moving averages across 250 and 75 sequential cells for progenitors and differentiating cells, respectively. Shading denotes bootstrapped 95% confidence interval for the moving average. Colors denote cell type.
(B-D) Expression dynamics and joint Pnt-Yan distributions for differentiating R8, R3/R4, and R7 cells. Joint distributions are limited to progenitor and R cells drawn from the vertically shaded region spanning the first ten R cells of the specified type in each disc. Solid lines are smoothed moving averages across 250 and 50 samples for progenitor and R cells, respectively.

212 If cell-to-cell variation in the Pnt-to-Yan ratio contributes to differentiative competence within the
213 progenitor population, then variability should rise to a maximum within the pool of progenitors from which
214 R cells are recruited, and then subside as fates are resolved. To test this, we adapted our reported
215 method (Peláez et al., 2015) to quantify simultaneously the dynamic cell-to-cell heterogeneity of Pnt
216 levels, Yan levels, and the Pnt-to-Yan ratio among both progenitors and R cells (Figure 2 - figure
217 supplement 2). Within the progenitor pool, a broad increase in cell-to-cell variation, quantified by the
218 coefficient of variation of the ratio, coincided with the time periods in which state transitions occurred.
219 Ratio variation was predominantly attributed to Yan and Pnt variability during the first and second waves
220 of R cell state transitions, respectively. Heterogeneity among progenitor cells decreased back to basal
221 levels after all R cell fate transitions were complete. Similar trends were evident among transitioning R
222 cells, but with a more rapid approach toward a consensus ratio following fate specification. We conclude
223 that an increase in the Pnt-to-Yan ratio marks, and perhaps initiates, the transition from progenitor to R
224 cell state, and that increased Pnt and Yan expression variability within the progenitor pool may ensure
225 adequate differentiative competence.

226 **Increasing or decreasing the Pnt-to-Yan ratio perturbs cell state transitions**

227 If cell state transitions in the developing retina rely on ratiometric sensing of relative Pnt and Yan
228 levels, then either increasing or decreasing the Pnt-to-Yan ratio should compromise photoreceptor
229 specification. We first tested this hypothesis by varying the genetic dosage of the *pnt* gene from one to
230 four copies. Animals with only one copy of *pnt* should have two-fold lower than normal Pnt-to-Yan ratios
231 while those with four copies of the gene should have two-fold higher than normal ratios. If such ratio
232 deviations are sufficient to compromise cell state transitions, then the respective photoreceptor loss and
233 ectopic specification should disrupt adult external eye morphology.

234 However, the eyes of the adult flies were morphologically indistinguishable from wild type across
235 this *pnt* dosage range (Figure 1 - figure supplement 1A,B). To confirm Pnt protein concentration was
236 indeed proportional to gene copy number, as it is for most *Drosophila* genes (Lucchesi and Rawls, 1973),
237 we quantified Pnt-GFP levels in eye cells containing one versus two copies of the *pnt-gfp* transgene in a
238 *pnt* mutant background. As expected, Pnt-GFP protein concentration varied proportionally to *pnt-gfp*
239 gene copy number (Figure 3A,B). Therefore, the absence of overt phenotypes suggested that either cell
240 state transitions are not sensitive to two-fold differences in ratio or that there are feedback mechanisms
241 that drive cells back to the ideal ratio.

242 We distinguished between these possibilities by measuring the Pnt-to-Yan ratio. We found that
243 average Yan protein concentration scaled with *pnt-gfp* gene copy number (Figure 3C,D) such that the

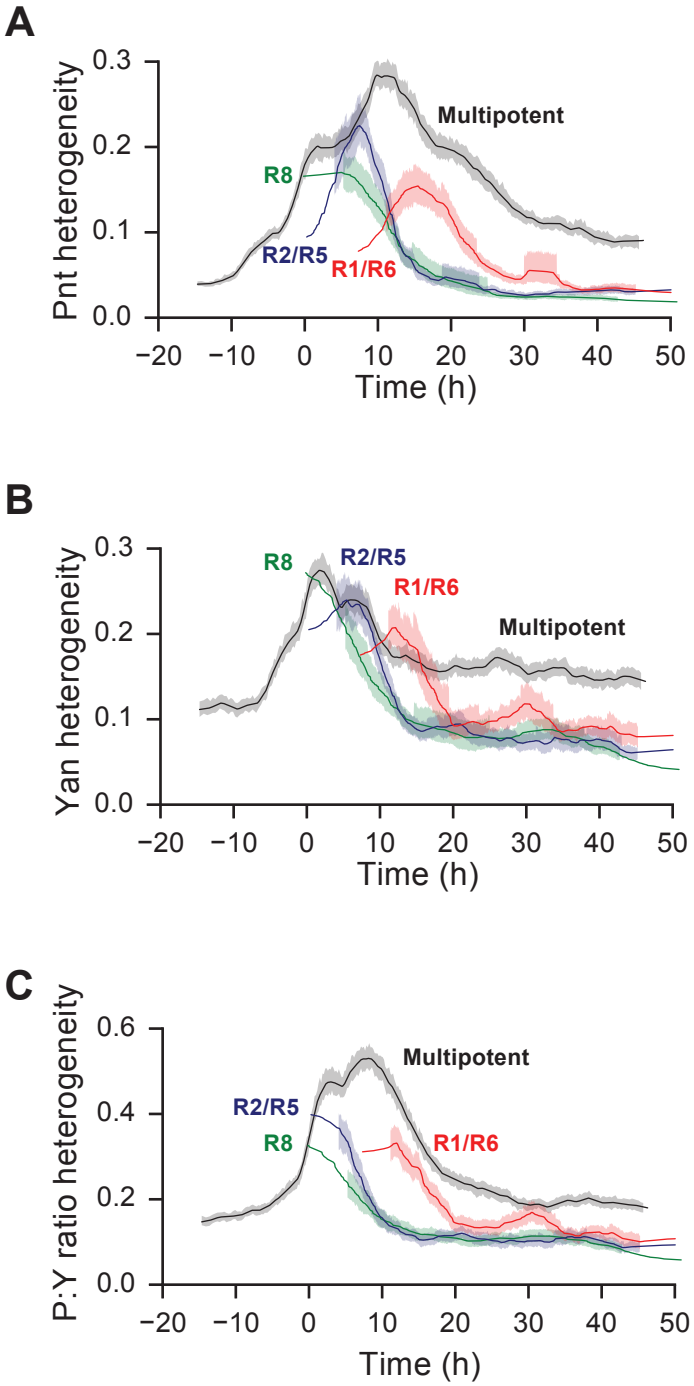

Figure 2 - figure supplement 2: Dynamics of expression variability in progenitor, R8, R2/R5, and R1/R6 cells. Heterogeneities of **(A)** Pnt expression, **(B)** Yan expression, and **(C)** the log2-transformed ratio are estimated by de-trending fluctuations about a moving average of 250 sequential cells. Lines are moving averages of 250 sequential fluctuations. Shaded regions are bootstrapped 95% confidence intervals for the moving average. Colors denote cell type.

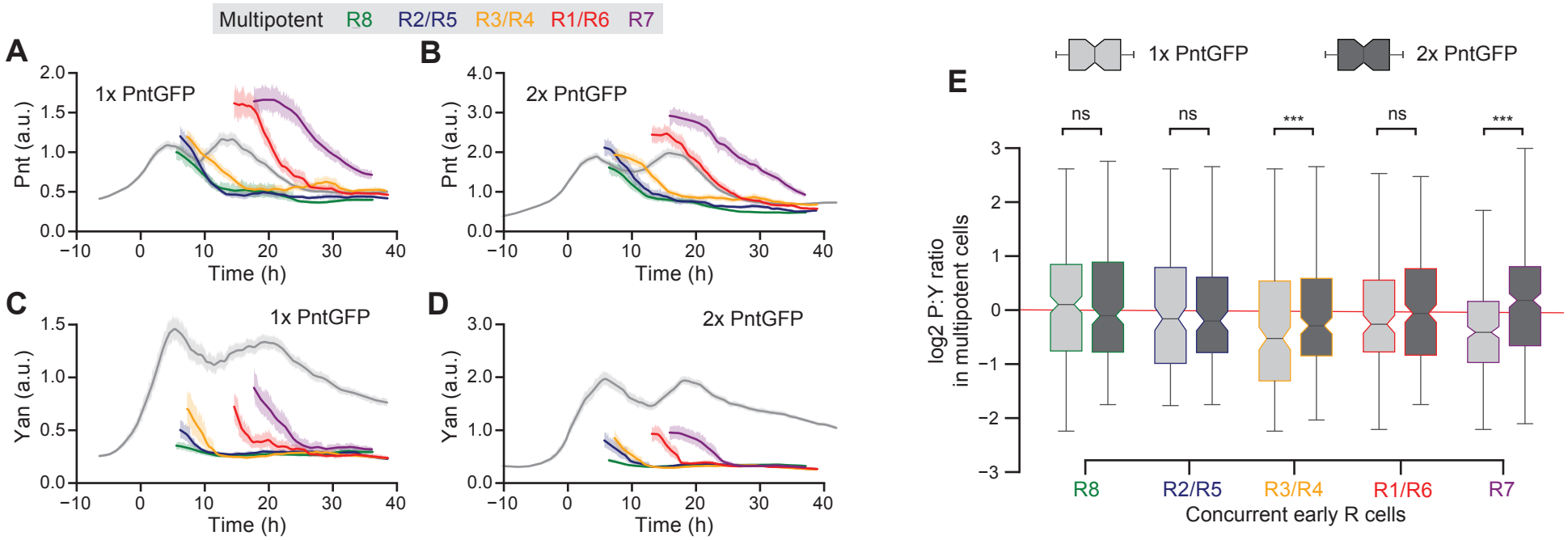

Figure 3: The Pnt-to-Yan ratio is stabilized against varying Pnt and Yan concentrations in progenitor cells.
(A-D) Moving averages of **(A, B)** Pnt-GFP and **(C, D)** Yan levels in progenitor and differentiating cells with one **(A, C)** versus two **(B, D)** copies of the *pnt-gfp* gene. Measurements used DAPI to mark nuclei. Colors denote cell type. Shaded regions are bootstrapped 95% confidence intervals for the moving average.
(E) Comparison of Pnt-to-Yan ratios between progenitor cells with one versus two copies of *pnt-gfp* during cell fate transitions. Colors denote cell fate transition periods for each R cell type. These time periods are defined in each disc by the times spanned by the first ten identifiable R cells. The concurrent progenitor cell populations are selected from these time windows. Light grey filled boxes denote 1x *pnt-gfp*, dark grey filled boxes denote 2x *pnt-gfp*. Pnt-to-Yan ratios in progenitor cells are indistinguishable between gene dosages during R8, R2/R5, and R1/R6 cell fate transitions (P>.1, KS 2-sample test).

244 Pnt-to-Yan protein ratio was not significantly changed (Figure 3E). This suggests that the network
245 compensates for variation in the abundance of Pnt by adjusting Yan protein levels, driving cells back
246 toward a set Pnt-to-Yan ratio. As a result, cell fate transitions are not perturbed. We imagine that
247 effective control of the Pnt-to-Yan ratio would require a similar dependence of Pnt protein levels on the
248 concentration of Yan. Consistent with this idea, prior studies reported that wild type eye development is
249 robust to either change in *yan* gene copy number (Peláez et al., 2015) or to overexpression of wild type
250 *yan* cDNA (Rebay and Rubin, 1995)

251 To test the functional significance of the ratio to cell fate transitions, we therefore needed to
252 introduce genetic perturbations that would both perturb the ratio and circumvent the system's ability to
253 compensate. Induced expression of constitutively active forms of either Ras or Yan provided appealing
254 strategies. Constitutively active Ras, Ras^{V12}, is stabilized in an active GTP-bound state and so
255 constitutively activates the downstream MAPK cascade to drive ectopic photoreceptor fate transitions
256 (Fortini et al., 1992; Karim et al., 1996; Rebay and Rubin, 1995). Constitutively active Yan, Yan^{ACT}, is
257 insensitive to MAPK phosphorylation induced degradation and blocks photoreceptor fate transitions
258 (Fortini et al., 1992; Karim et al., 1996; Rebay and Rubin, 1995). We hypothesized that these two fate
259 transition phenotypes would be associated with respective increases or decreases in Pnt-to-Yan ratios.

260 For our experiments we expressed Ras^{V12} and Yan^{ACT} as cDNA transgenes under direct control
261 of the enhancer/promoter of the *sevenless* (*sev*) gene (Fortini et al., 1992; Rebay and Rubin, 1995;
262 Simon et al., 1991). The *sev* gene is transiently expressed in a subset of progenitor cells posterior to the
263 MF and during the transitions that lead to R7, R3 and R4 fates (Banerjee et al., 1987; Raabe, 2000;
264 Tomlinson et al., 1987). A major advantage of using *sev*-driven overexpression of Ras^{V12} and Yan^{ACT} is
265 that events that establish R8 spacing and initiate other R cell transitions are not disrupted, allowing us to
266 identify individual cell types. Crossing to a UAS-mCherryNLS reporter line confirmed *sev-Gal4* drives
267 expression in the expected pattern (Figure 4 - figure supplement 1).

268 When we compared Yan and Pnt-GFP expression dynamics in progenitor cells of wild type
269 versus *sev-*Ras^{V12} eye discs, we found that constitutive Ras activity dramatically increased the amplitude
270 and duration of the second peak of Pnt-GFP expression (Figure 4A) but did not significantly alter Yan
271 expression dynamics (Figure 4B). The lack of change in Yan levels suggests that if the system "tried" to
272 compensate for the increase in Pnt levels by increasing Yan production, the sustained MAPK activation
273 induced by Ras^{V12} prevented excess Yan accumulation. The end result was a sustained increase in Pnt-
274 to-Yan ratio in progenitors during and after the second wave of state transitions (Figure 4C). Ectopic
275 specification of R cells was also noted, though their identities could not be discerned due to their

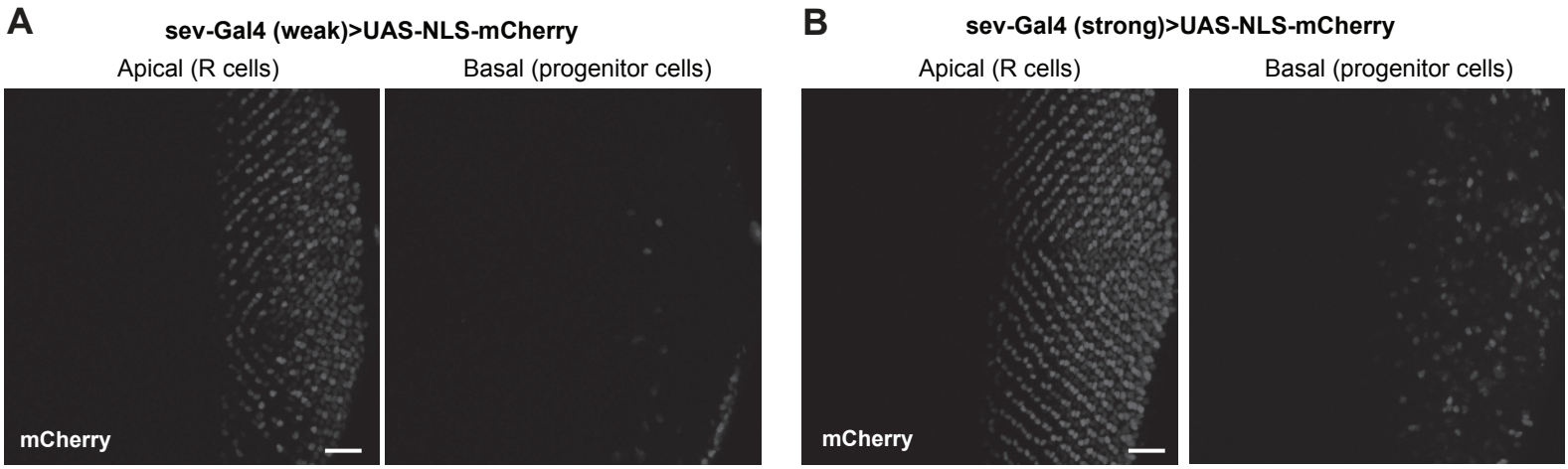

Figure 4 - figure supplement 1: Strong but not weak Sev>Gal4 drives expression in progenitors.
(A, B) Maximal projection of mCherry signal in apical z-slices containing R cell nuclei (left) and basal z-slices containing progenitor cells (right) of **(A)** weak sev-Gal4>UAS-NLS-mCherry and **(B)** strong sev>Gal4>UAS-NLS-mCherry. Scale bar denotes 20 μm. When driven by the weak promoter, mCherry expression is predominantly limited to R7, R3, and R4 cells. When driven by the strong promoter, mCherry is also expressed among some progenitor cells.

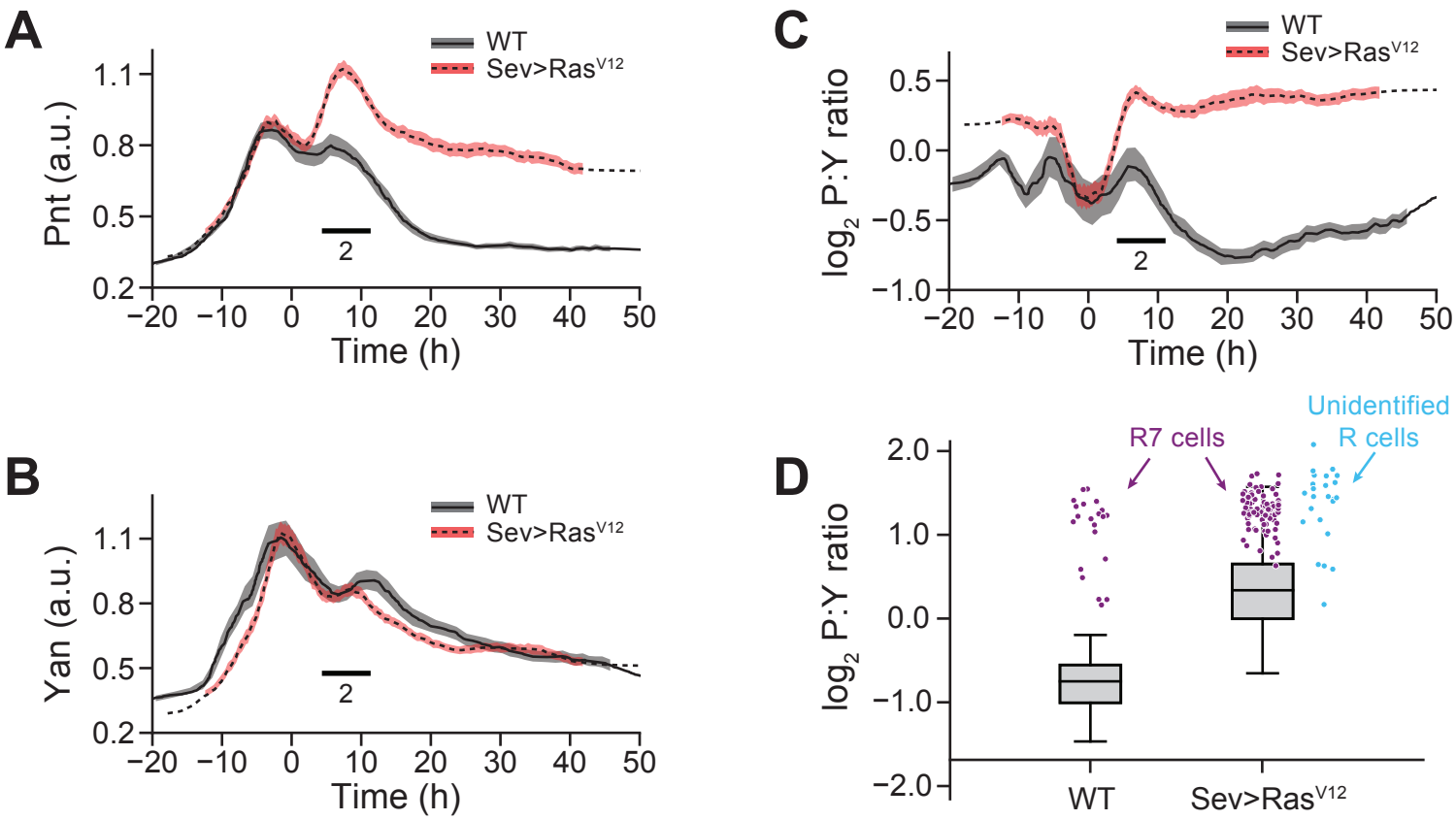

Figure 4: Ras signaling elevates the Pnt-to-Yan ratio in progenitor cells. See figure supplements 1 and 2.
(A-C) Effects of constitutive Ras^{V12} signaling on **(A)** Pnt-GFP, **(B)** Yan, and **(C)** the Pnt-to-Yan ratio in progenitor cells. Lines are moving averages across 250 sequential cells. Shaded regions are bootstrapped 95% confidence intervals for the mean. Solid lines and grey shading denote wildtype controls. Dashed lines and red shading denote constitutive Ras signaling by sev>Ras^{V12}. Black bars denote periods of elevated Pnt-GFP expression. We previously reported a modest increase in the duration of Yan-YFP expression in sev>Ras^{V12} mutant progenitor cells (Peláez et al. 2015), but this difference was not detected using the Yan antibody.
(D) Comparison of Pnt-to-Yan ratios between wildtype and sev>Ras^{V12} progenitor cells concurrent with the ectopic differentiation of unidentified R cells in sev>Ras^{V12} discs. Light blue markers denote the first 25 supernumerary R cells. Purple markers denote the concurrent R7 cells.

276 aberrant positions (Figure 4 - figure supplement 2A,B), consistent with prior descriptions of the
277 *sev>Ras*^{V12} phenotype (Fortini et al., 1992; Karim et al., 1996). As a result of the excessive
278 photoreceptor recruitment, the progenitor pool in the most posterior region of the eye disc was noticeably
279 depleted relative to wild type.

280 If the measured ratiometric imbalance was responsible for the ectopic fate transitions, then the
281 supernumerary R cells should emerge from a pool of progenitors with abnormally high Pnt-to-Yan ratios.
282 Focusing our analysis on progenitor cells that were temporally concurrent with the induction of ectopic R
283 cells, we found that their ratios were higher than those of wildtype progenitor cells at comparable times
284 (Figure 4D grey boxes). Many young supernumerary R cells had ratios that were within the range of
285 mutant progenitor cells (Fig. 4D blue dots). Similar to the concurrent populations of wildtype and mutant
286 R7 cells (Fig. 4D purple dots), nearly all supernumerary R cells were above the range observed in
287 wildtype progenitors. This suggests that abnormally high Pnt-to-Yan ratios in progenitor cells accompany,
288 and perhaps drive, ectopic R cell state transitions.

289 Just as high ratios trigger state transitions, abnormally low Pnt-to-Yan ratios should prevent them.
290 To test this, we quantified Yan and Pnt-GFP expression dynamics in *sev-Yan*^{ACT} eye discs. In contrast to
291 the results with the *sev>Ras*^{V12} experiment, no changes in Pnt or Yan levels were detected in the
292 progenitor pool (Figure 5A-C). Concerned that the level of overexpression might be insufficient to
293 perform the intended experiment, we increased Yan levels further using *sev-Gal4>UAS*-Yan^{ACT}
294 expression. Although elevated Yan levels were now readily detected in the progenitor pool, the
295 disruptions to ommatidial patterning that resulted from the ensuing R cell loss were too severe to permit
296 quantitative analysis.

297 Returning to the milder *sev-Yan*^{ACT} background, although average Yan levels in the progenitor
298 pool were not detectably elevated, a striking reduction in R7 fates was noted, with 85% of ommatidia
299 failing to specify R7 cells (Figure 5D,E). To explain the R7 loss, we focused on cells five to ten hours
300 after the initial onset of R7 specification, reasoning that this should allow sufficient time for ectopic Yan
301 accumulation. The few remaining R7s in this region showed comparable Pnt-to-Yan ratios to the
302 concurrent population of progenitor cells, in stark contrast to the elevated ratios among R7s in the wild
303 type control (Figure 5F and Figure 5 - figure supplement 1A,B). Comparison of Yan and Pnt-GFP
304 expression confirmed that the reduced ratio during the attempted R7 transition was driven primarily by
305 increased Yan levels in *sev-Yan*^{ACT} cells relative to wild type (Figure 5 - figure supplement 1C). Scoring
306 mature photoreceptor cell fates in the adult retina revealed almost complete loss of R7s (Figure 4 - figure

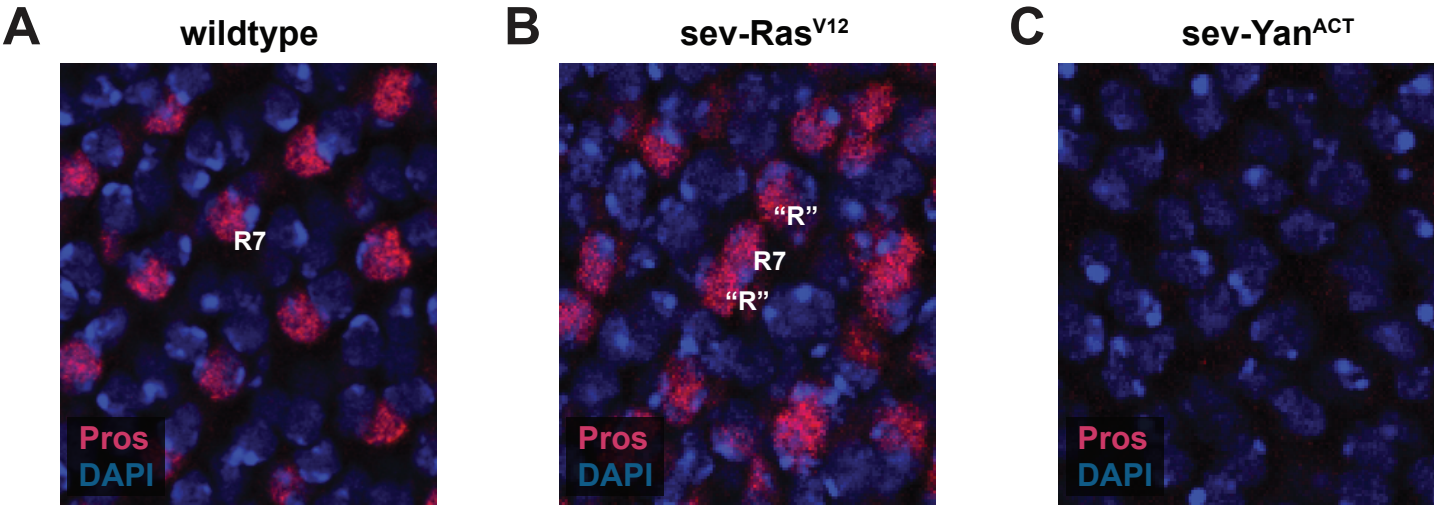

Figure 4 - figure supplement 2. R7 phenotype in sev>Ras^{V12} and sev>Yan^{ACT}.
Antibody staining of Prospero in 9-10 ommatidia in the equivalent posterior region of the eye disc in **(A)** wildtype, **(B)** sev>Ras^{V12}, and **(C)** sev>Yan^{ACT} animals. R7 cell is marked based on stereotypical nuclear position. Extra R cells on each side of the R7 are marked as "R" in the sev>Ras^{V12} disc.

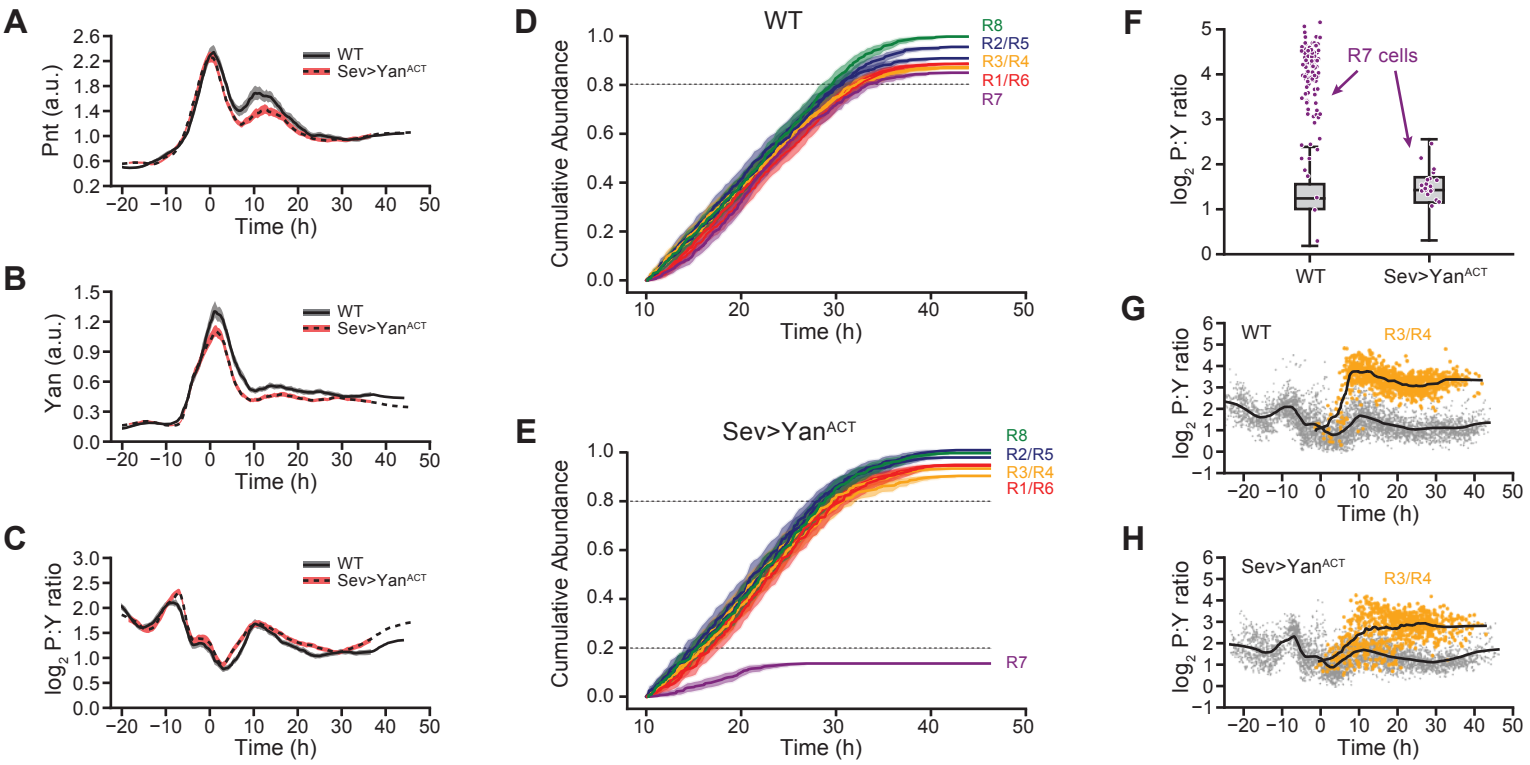

Figure 5: Constitutive Yan expression decreases the Pnt-to-Yan ratio in R7, R3, and R4 cells. See figure supplements 1 and 2.

(A-C) Effects of constitutive Yan expression on **(A)** Pnt-GFP, **(B)** Yan, and **(C)** the Pnt-to-Yan ratio in progenitor cells. Lines are moving averages across 250 sequential cells. Shaded regions are bootstrapped 95% confidence intervals for the mean. Solid lines and grey shading denote wildtype controls. Dashed lines and red shading denote constitutive Yan expression by *sev>Yan-ACT*.

(D, E) Cumulative abundance of each annotated R cell type as a function of developmental time in **(D)** wildtype and **(E)** *sev>Yan-ACT* discs. Contours are normalized by the total number of R8 cells detected across the time-course, and R2, R5, R3, R4, R1, and R6 cells are each tallied separately. Colors denote R cell type. Shading denotes bootstrapped 95% confidence intervals for each contour. R7 cells were not detected in approximately 85% of *sev>Yan^ACT* ommatidia.

(F) Comparison of Pnt-to-Yan ratios between wildtype and *sev>Yan^ACT* progenitor cells concurrent with remaining R7 cells in *sev>Yan^ACT* discs. Plot includes all multipotent and R7 cells between 15 and 20 h of developmental time. Purple markers denote the R7 cells for each genotype.

(G, H) Measured Pnt-GFP-to-Yan ratio dynamics among multipotent and R3/R4 cells in **(G)** wildtype and **(H)** *sev>Yan^ACT* discs. Solid lines are moving averages across 250 and 75 sequential cells for progenitors and R3/R4 cells, respectively. Grey markers represent multipotent cells.

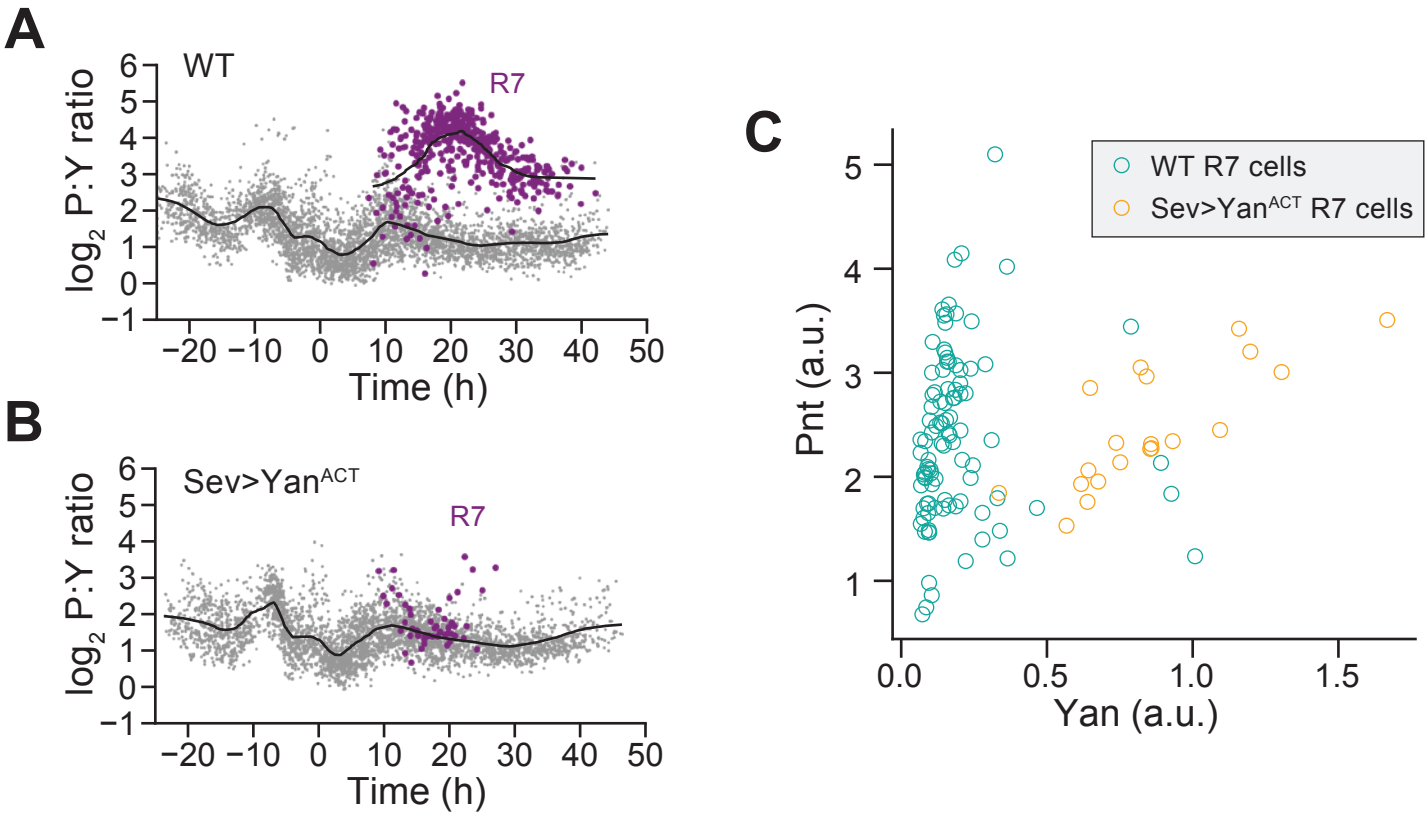

Figure 5 - figure supplement 1: Elevated Yan^{ACT} levels suppress the Pnt-to-Yan ratio in R7 cells.
(A, B) Measured Pnt-GFP-to-Yan ratio dynamics among multipotent and R7 cells in **(A)** wildtype and **(B)** *sev>yan^{ACT}* discs. Solid lines are moving averages across 250 and 75 sequential cells for progenitors and R7 cells, respectively. Grey markers represent multipotent cells.
(C) Joint distribution of measured Pnt and Yan levels among R7 cells sampled from the region spanning 15 to 20 h of developmental time. The *sev>yan^{ACT}* R7 cells showed higher Yan levels (P<.001, KS 2-sample test), while Pnt levels were indistinguishable from wildtype (P=.4, KS 2-sample test).

307 supplement 2C), firmly connecting the failed fate transition to the inability of Yan^{ACT} expressing R7 cells
308 to elevate the Pnt-to-Yan ratio.

309 When we looked at the other photoreceptor fates, R8, R2/R5 and R1/R6 fate transitions appeared
310 normal and were marked by wild type Pnt-to-Yan expression and ratio dynamics (Figure 5 - figure
311 supplement 2). However, perturbed ratio dynamics were apparent in young R3/R4 cells. In wild type
312 discs, young R3/R4 cells with ratios equivalent to those of concurrent progenitors were identified just
313 before the second peak of Pnt-GFP expression, but immediately posterior almost all R3/R4 cells had
314 ratios that were significantly elevated relative to those of their concurrent progenitors (Figure 5G). In
315 contrast, in *sev-Yan^{ACT}* eye discs, there was a delay in elevating Pnt-to-Yan ratios in the R3/R4
316 population relative to the concurrent progenitor pool (Figure 5H). However, in older ommatidia of *sev-*
317 *Yan^{ACT}* eye discs, mature R3/R4 cells were present and had stable elevated Pnt-to-Yan ratios, similar to
318 wild type. Examination of adult *sev-Yan^{ACT}* eyes confirmed only a slight loss of R3/R4 fates. This
319 suggests that the delay in elevating the Pnt-to-Yan ratio in the R3/R4 progenitor pooled delayed but did
320 not block the fate transition.

321 **Cooperative DNA-binding sensitizes enhancer occupancy to changes in Pnt-to-Yan ratio**

322 How could cells reprogram transcription in response to a change in the Pnt-to-Yan ratio across a
323 wide range of absolute protein concentrations? Since both Pnt and Yan are ETS family transcription
324 factors with overlapping sequence specificity for DNA binding (Flores et al., 2000; Halfon et al., 2000;
325 Lachance et al., 2018; Nitta et al., 2015; Webber et al., 2013a, 2013b; Wei et al., 2010; Xu et al., 2000;
326 Zhu et al., 2011), the underlying mechanism may reflect competition for binding sites in target gene
327 enhancers. Illustrating this point, a simple model in which two transcription factors compete for
328 occupancy shows that if the sites are saturated, then equilibrium occupancy by either factor is more
329 sensitive to the relative concentration of the two factors than to the absolute concentration of both
330 species (Figure 6 - figure supplement 1).

331 However, the situation is more complex for Pnt and Yan. While there are several well-
332 documented target genes that contain enhancers with common binding sites for Pnt and Yan (Flores et
333 al., 2000; Halfon et al., 2000; Xu et al., 2000), Yan binds these sequences with higher affinity than Pnt
334 (Xu et al., 2000). Moreover, recent experiments suggest Yan and Pnt differentially interpret the structural
335 syntax of cis-regulatory modules (Lachance et al., 2018). This complex phenomenon is a consequence
336 of cooperative interactions between DNA-bound Yan molecules. Specifically, Yan monomers are able to
337 self-associate via their sterile alpha motifs (SAM), enabling DNA-bound Yan monomers to stabilize the
338 recruitment of additional Yan monomers to adjacent sites (Lachance et al., 2018; Qiao et al., 2004a;

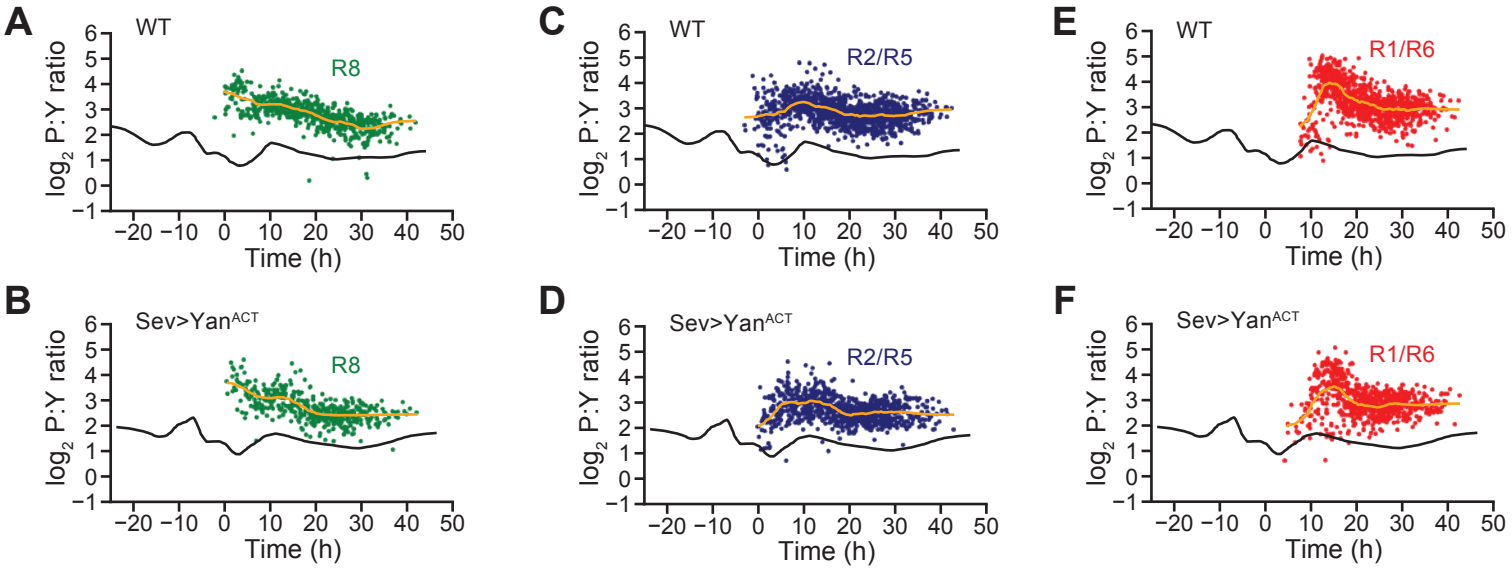

Figure 5 - figure supplement 2: Yan^{ACT} has little effect on Pnt-to-Yan ratio dynamics in R8, R2, R5, R1, or R6 cells. **(A-F)** Measured Pnt-GFP-to-Yan ratio dynamics among differentiating R cells in wildtype (top row) and *sev>yan^{ACT}* (bottom row) eye discs. Solid black and yellow lines are moving averages across 250 and 75 sequential cells for progenitors and R7 cells, respectively. Colors denote R cell type.

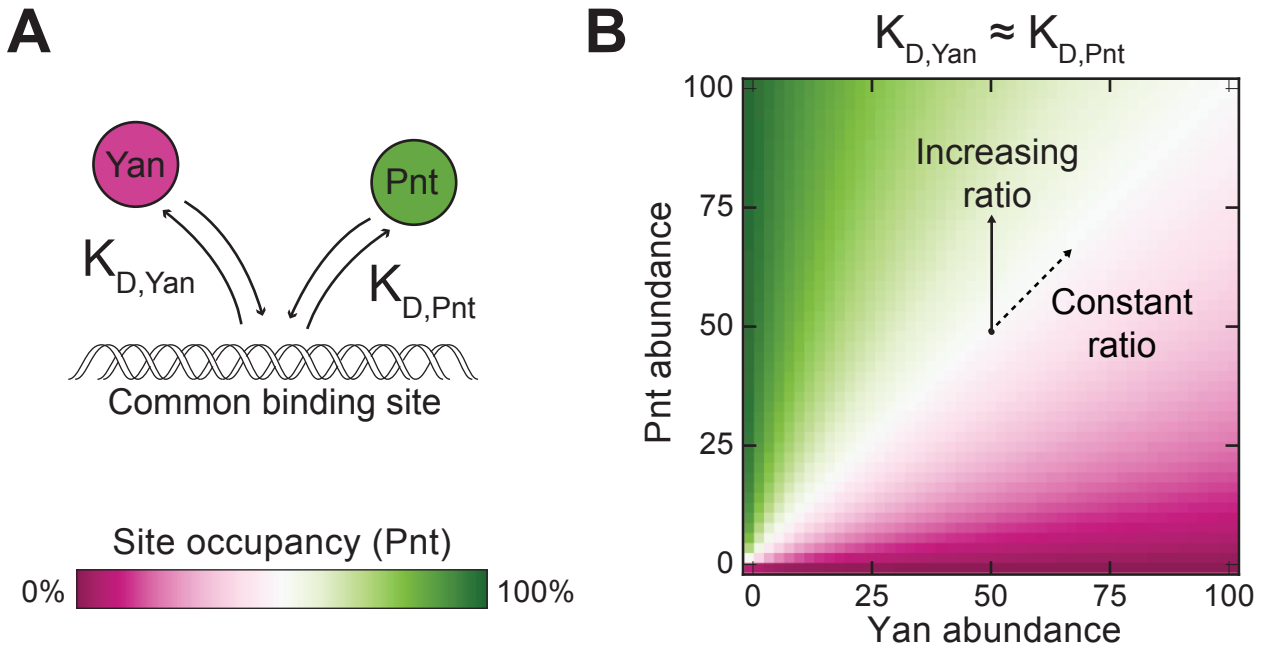

Figure 6 - figure supplement 1: A simple competitive binding model.
(A) Schematic of a simple two-species competitive binding model.
(B) Theoretical Pnt site occupancy as a function of transcription factor abundance. Equivalent binding affinities are used for illustrative purposes. Simultaneous proportional increases in absolute abundance of both species have minimal impact on Pnt occupancy, while varying ratio confers maximal change.

339 Zhang et al., 2010) Because Pnt does not self-associate (Mackereth et al., 2004; Meruelo and Bowie,
340 2009), Yan-Yan cooperativity could bias the competition.

341 To consider this possibility, we adapted a modeling framework developed to probe the effects of
342 *cis*-regulatory syntax on Yan binding site occupancy (Hope et al., 2017). The model considers an
343 ensemble of microstates, each defined by a unique configuration of vacant or Yan-bound sites. Each
344 microstate is assigned a thermodynamic potential based on the cumulative influence of strong sequence-
345 specific binding to consensus ETS sites, weak non-specific DNA binding, and SAM-SAM polymerization.
346 We augmented this model by incorporating Pnt as a second transcription factor that competes for
347 occupancy of the same binding sites but does not self-associate (Figure 6 - figure supplement 2A,B).
348 Using this model, we explored how Yan-Yan cooperativity might impact the sensitivity of Pnt binding site
349 occupancy to changes in the Pnt-to-Yan ratio.

350 We first considered a scenario in which neither Yan nor Pnt exhibit cooperativity (Figure 6A). In
351 the absence of stabilizing SAM-SAM interactions, the landscape of overall binding site occupancy was
352 identical to that obtained with the simple binding model described above (Figure 6 and Figure 6 - figure
353 supplement 1). Increasing the Pnt-to-Yan ratio resulted in a gradual increase in Pnt occupancy for all
354 individual binding sites, producing a titration contour closely resembling a Michaelis-Menten saturation
355 curve (Figure 6C).

356 Introducing a stabilizing SAM-SAM interaction for Yan (Figure 6D) sharpened the transition from
357 Yan to Pnt occupancy dominance (Figure 6E). Weighting the energetic contributions of binding strength
358 and polymerization by the statistical frequency of each microstate revealed that the transition was driven
359 by an abrupt change in the dominant binding mechanism. Polymerization-associated cooperativity effects
360 dominate binding site occupancy when the Pnt-to-Yan ratio is low, while binding strength dominates
361 when the ratio is high (Figure 6 - figure supplement 2C).

362 Increasing the Pnt-to-Yan ratio revealed nonlinear transitions from low to high Pnt occupancy for
363 each individual binding site (Figure 6F). These transitions resembled Hill function forms, with sharp
364 thresholds delimiting distinct transcriptional outputs. At low Pnt-to-Yan ratios, Yan occupancy dominated,
365 while at some critical Pnt-to-Yan ratio, Pnt-bound molecules prevented Yan-Yan interactions, ultimately
366 allowing Pnt to outcompete Yan as the ratio increased further. Assuming binding sites are saturated,
367 then relative occupancy by Pnt and Yan should be agnostic to changes in the absolute abundance of
368 either factor, as long as the Pnt-to-Yan ratio remains constant. This mechanism, coupled with
369 cooperativity, would enable modest changes in the Pnt-to-Yan ratio to elicit large changes in DNA

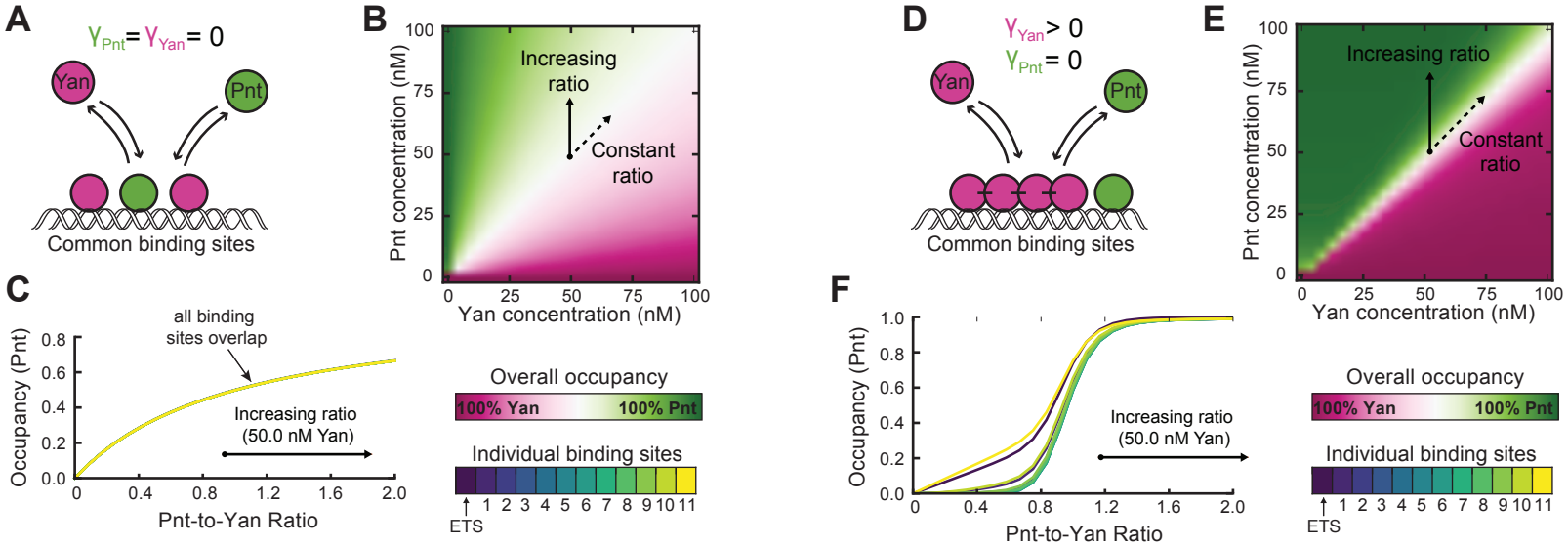

Figure 6: Cooperative DNA-binding sensitizes transcriptional output to the Pnt-to-Yan ratio. See figure supplements 1 and 2.
(A) Cartoon of competition between Pnt and Yan for occupancy of mutual binding sites in the absence of Yan polymerization. Also see figure supplement 1.
(B) Overall binding site occupancy as a function of transcription factor abundance in the absence of Yan polymerization. Color scale reflects overall Pnt site occupancy. A diverging scale was used because all sites are fully saturated at total transcription factor concentrations above 1 nM. Under the range of conditions shown, this implies that Yan occupies all sites left vacant by Pnt. Simultaneous proportional increases in absolute abundance of both species have minimal impact on Pnt occupancy (dashed arrow), while varying ratio confers gradual change (solid arrow).
(C) Pnt occupancy of individual binding sites as a function of Pnt-to-Yan ratio in the absence of Yan polymerization. Contours correspond to a vertical path traversed across panel B at a fixed Yan concentration of 50 nM. All binding sites behave similarly.
(D) Cartoon of competition between Pnt and Yan for occupancy of mutual binding sites when Yan polymerizes via its SAM domain.
(E) Overall binding site occupancy as a function of transcription factor abundance when Yan polymerizes via its SAM domain. Color scale and arrows retain their meaning from panel B.
(F) Pnt occupancy of individual binding sites as a function of Pnt-to-Yan ratio when Yan polymerizes via its SAM domain. Contours correspond to a vertical path traversed across panel E at a fixed Yan concentration of 50 nM. Line colors reflect binding site positions within the cis-regulatory element. Sites at intermediate distances from the strong ETS site (green lines) transition at higher ratios than those nearest and furthest from the strong ETS site (blue and yellow lines).

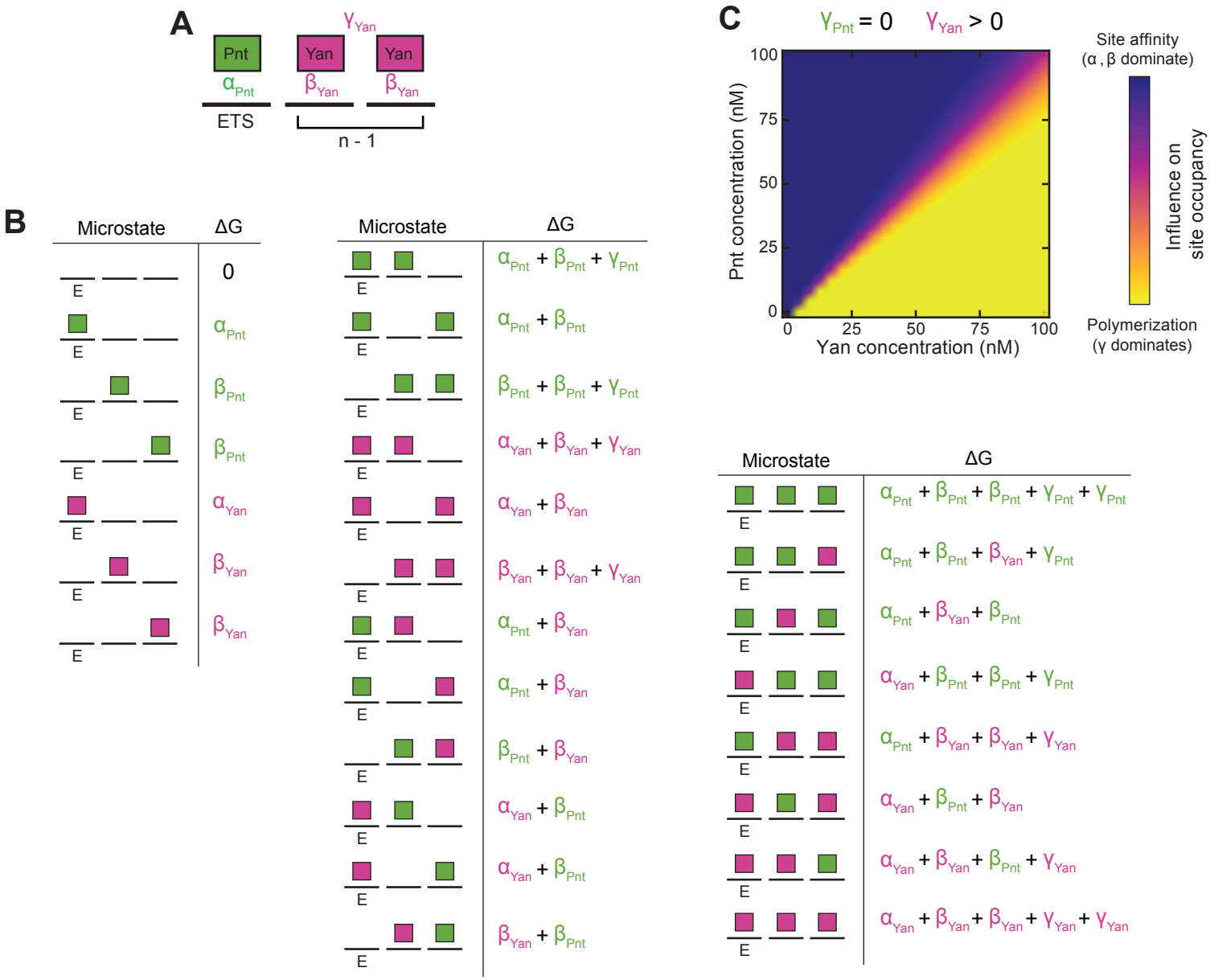

Figure 6 - figure supplement 2: A statistical physics model for Yan / Pnt binding.

(A) Summary of thermodynamic interactions within one microstate of a cis-regulatory element containing one ETS site and two non-ETS sites. Solid black lines represent individual binding sites. Green and magenta rectangles denote Pnt and Yan molecules. Example thermodynamic potentials of strong ETS-binding, weak non-ETS binding, and polymerization interactions are denoted by α_{Pnt}, β_{Yan}, and γ_{Yan}, respectively. For this microstate, $a_P(k)$=1 and $a_Y(k)$=2.

(B) Enumeration of all possible microstates for a cis-regulatory element of length 3 in which only the first site carries the ETS designation. Solid black lines denote binding sites, green and magenta rectangles denote bound Pnt and Yan molecules. The cumulative thermodynamic potentials of each microstate, ΔG_k, are listed beside each graphical depiction.

(C) Relative thermodynamic contributions of binding site affinity versus polymerization to microstate statistical frequencies as a function of Pnt and Yan concentration. For each point in the plane, influence of site affinity was calculated by weighting the sum of all ETS and non-ETS thermodynamic potentials for each microstate by the statistical frequency of the corresponding microstate. The influence of polymerization was analogously determined. The shown color scale reflects the relative magnitude of these two summations, normalized by limits of zero and complete polymerization.

370 binding site occupancy by either factor, with the presumably large changes in target gene mRNA
371 synthesis resulting in a state transition.

372

373 **DISCUSSION**

374 We have identified a scenario in which cell state transitions are best defined by changes in the
375 relative abundance of the activator/repressor pair Pnt and Yan, rather than by the absolute concentration
376 of either transcription factor. Our results suggest that cells maintain a fixed Pnt-to-Yan ratio in the
377 progenitor pool, and that RTK/MAPK signaling overcomes the buffering mechanism that maintains the
378 ratio at that fixed point. This produces a sustained increase in the ratio that marks, and perhaps drives,
379 the transition to specified photoreceptor (R) fates. Consistent with this interpretation, genetic
380 perturbations that disrupt the ratio produce cell fate specification defects. Mathematical modeling
381 suggests that changes in the Pnt-to-Yan ratio will promote functionally distinct transcriptional complexes
382 at target gene enhancers, with lower Pnt-to-Yan ratios favoring repressive Yan-dominated complexes
383 and higher ratios producing Pnt-dominated activating complexes. In this way, the RTK/MAPK signal
384 triggers a molecular switch that reliably activates previously repressed gene expression programs to
385 drive the differentiative transition.

386 Successful cell state transitions usually require specific changes in mRNA and protein
387 expression, which are often dictated by transcription factors. It is widely believed that developmental
388 gene expression programs depend on the absolute concentration of the transcription factors that control
389 them (Spitz and Furlong, 2012). Our study in the developing *Drosophila* eye has revealed a different
390 mechanism whereby cells respond to changes in the ratio in abundance of two transcription factors
391 rather than to changes in the absolute concentration of either protein.

392 Two key characteristics of the Pnt/Yan system make ratiometric control of cell state transitions
393 possible. First, both factors bind to the same DNA sites in the target genes but exert opposing effects on
394 transcription. Gene targets associated with specific photoreceptor fates are repressed in progenitors
395 where the Pnt-to-Yan ratio is low and transcriptionally activated when eye cells transit to differentiated
396 states in response to increased ratio; induction of target gene expression is necessary for differentiation
397 (Nagaraj et al., 2002; Xu et al., 2000). Second, stabilizing interactions between adjacently bound Yan
398 monomers sensitize enhancer occupancy to the relative abundance of the competing transcription
399 factors. As was first shown for the human ortholog of Yan, TEL1 (Green et al., 2010; Kim et al., 2001),
400 DNA-bound Yan monomers enhance recruitment of Yan to adjacent binding sites through stabilizing

401 SAM-SAM polymerization (Lachance et al., 2018; Qiao et al., 2004a). Such cooperativity could generate
402 threshold-like behavior and cause an ultrasensitive switch in site occupancy between Yan and Pnt.

403 Under these conditions, relative site occupancy by either factor determines whether or not a
404 target gene is transcribed. Our modeling predicts that when binding sites are saturated, the probability a
405 site is occupied by one of the factors is controlled by the ratio of factor concentrations and not by the
406 absolute concentration of the factors. In other words, as long as the relative Pnt-to-Yan ratio is precisely
407 controlled, the downstream transcriptional switches that define retinal cell state transitions should be
408 agnostic to the absolute abundance of either transcription factor. Indeed, our experimental results
409 revealed the existence of a feedback control mechanism that can maintain the optimal ratio over at least
410 a four-fold range in transcription factor level. In this way, state transitions can proceed reliably despite
411 variation in protein concentrations driven by fluctuations in metabolism, cell volume, expression noise,
412 environment, genetic polymorphisms, or gene copy number.

413 This mechanism also explains how the transcription factors can have pulsatile expression
414 dynamics in eye progenitor cells, be co-expressed, and still consistently regulate transcription.
415 Regulation of genes through pulsatile dynamics of competing transcription factors with opposing effects
416 has been reported in yeast (Lin et al., 2015). However, in the developing eye, this competition relies on
417 the ratio of the two factors to differentially regulate gene transcription. Perhaps the pulsatile dynamics of
418 Pnt and Yan restrict R cell state transitions to the specific period of developmental time of the late third
419 instar larval stage. Identification of the transcriptional and post-transcriptional mechanisms that initiate
420 and maintain Yan and Pnt expression dynamics will be needed to explore this idea further.

421 Mechanistic studies in the embryonic mesoderm have shown that not only are Pnt and Yan co-
422 expressed, but that they can co-occupy enhancers and together may organize repressive transcriptional
423 complexes that poise target genes for activation (Webber et al., 2018). Although the chromatin
424 immunoprecipitation assays used in that study lacked the single cell and temporal resolution to
425 determine whether occupancy patterns changed during and after a transition, the assumption is that
426 RTK/MAPK signaling would shift the system toward Pnt-dominated occupancy and activation of gene
427 expression. If the same holds true in developing retinal cells, then the constant ratio in the progenitors
428 may maximize the probability that transcriptional complexes with the correct Pnt/Yan stoichiometry will
429 assemble to provide both the stabilizing repressive regulation and the requisite signal-responsiveness
430 needed to render a transition. Molecularly, state transitions require a switch from repression to activation
431 of transcription of a particular gene, and so the increase in Pnt-to-Yan ratio is likely to foster assembly of
432 transcriptional complexes with different stoichiometry.

The average Pnt-to-Yan ratio is dynamically stable within cells that remain in a particular state, and only exhibits transient change when cells switch states. These dynamics reflect the capacity of the system to coordinate the relative expression of the two transcription factors. Our results predict a stabilizing mechanism that monitors the relative abundance of Pnt and Yan and takes corrective action when the ratio deviates from a specified reference value. Although the ratio value is constant within either multipotent progenitor cells or R cells, the ratio value differs between progenitors and R cells. Hence, the stabilizing mechanism must be modified when cells change state in order to accommodate a sustained change in the ratio's set point. The precise nature of the stabilizing mechanism and the means by which it is modified are currently unknown and may include regulation not only at the transcriptional level, but also at all steps in protein synthesis and stability. Further complexity stems from the fact that the Pnt-GFP gene used in our study reports expression of the three protein isoforms that are required in different combinations to specify R2-R5 versus R1,R6 and R7 fates (Wu et al., 2020). Therefore, the ratiometric control mechanism must establish, measure and adjust levels of all three Pnt isoforms.

There are two time-windows when progenitor cells exhibit greater dispersion in their Pnt-to-Yan ratio. These time-windows correspond to the periods when a subset of the progenitor cells transit to R cell states. Thus, the mechanism that stabilizes the ratio at the progenitor fixed point is transiently overridden and the ratio values become highly heterogeneous. Many progenitors at this time have elevated ratios that overlap in value with those in committed R cells. It is possible that some of these high ratio progenitor cells are actually transiting across fates at that time but cannot yet be definitively identified as R cells. It is also possible that not all progenitors with elevated ratios transit to an R cell state, and that if they do not, their ratio values decline to the previous set point. In this sense, the progenitor cells might undergo transient fluctuations in ratio, with only some cells transiting their fate and maintaining an elevated ratio. Using live imaging to track Yan and Pnt levels in individual cells as they navigate these state transitions should help resolve these different possibilities.

In conclusion, we propose that an elevated Pnt-to-Yan ratio may be a requirement for retinal cells to transit to a stably specified state, and that reduced ratios can make these transitions less robust. While the ratiometric-based mechanism we have uncovered could be a unique feature of the repetitive waves of stereotyped cell state transitions that occur in the developing *Drosophila* eye, it may operate in other contexts in which progenitors co-express Pnt and Yan. Even more broadly, ratiometric control may prove to be a common and effective developmental strategy for ensuring the accuracy and robustness of cell state transitions that are regulated by combinatorial transcriptional inputs.

465 **METHODS**

466 **Genetics:**

467 Unless otherwise noted, all experiments were performed with animals reared at 25°C on standard
468 cornmeal-molasses Drosophila culture medium.

469 Fly stocks from the Bloomington Stock Center: *pnt-gfp* BAC transgene, BL42680; pnt^{2}, BL2222; *H2Av-*
470 *mRFP*, BL23651; w^{1118}, BL6326; UAS-mCherryNLS, BL38424. Additional alleles: $pnt^{\Delta 88}$ (O'Neill et al.,
471 1994); $sev{>}Ras^{v12}$(Fortini et al., 1992) ; $sev{>}Yan^{ACT}$ (Rebay and Rubin, 1995); *sev>Gal4* (Jemc and
472 Rebay, 2006).

473 Experiments measuring wild type dynamics of *Pnt-GFP* were done by dissecting eye discs from w^{1118} *;*
474 *pnt-gfp;* $pnt^{\Delta 88}/pnt^{2}$*, H2Av-mRFP* white prepupae. The effect of *pnt* gene dosage on Pnt-to-Yan ratio was
475 measured in w^{1118} ; *pnt-gfp /+ ;* $pnt^{\Delta 88}/pnt^{2}$ (1x *pnt*) and w^{1118} *; pnt-gfp;* $pnt^{\Delta 88}/pnt^{2}$ (2x *pnt*) discs.

476 In experiments with constitutive Ras or Yan activation, Pnt-GFP and Yan levels were measured in eye
477 discs from animals of the following genotypes: w^{1118} ; *pnt-gfp/* $Sev{>}Ras^{v12}$*;* $pnt^{\Delta 88}$/+ relative to w^{1118} ; *pnt-*
478 *gfp / +;* $pnt^{\Delta 88}$/+ wild type control; and w^{1118} ; *pnt-gfp/*$Sev{>}Yan^{ACT}$*;* $pnt^{\Delta 88}$/+ relative to w^{1118} ; *pnt-gfp / +;*
479 $pnt^{\Delta 88}$/+ wild type control.

480

481 **Immunohistochemistry**

482 For all experiments, eye-antennal discs were dissected from white prepupae. For experiments in
483 which 4′,6-diamidino-2-phenylindole (DAPI) was used as the nuclear marker, samples were fixed in 4%
484 paraformaldehyde (w/v) / PBS-Triton X-100 0.1% for 25 minutes at room temperature. After fixation, eye
485 discs were blocked in PBS-Triton X-100 0.1% and 1% normal goat serum for 30 minutes at room
486 temperature. Primary and secondary antibodies were incubated each for 2 hours at room temperature
487 with DAPI. Including DAPI during primary and secondary antibody staining was important for even
488 penetration of DAPI. Antibodies used: mouse anti-Yan 8B12 (DHSB, 1:200) and goat anti-mouse Cy3
489 (1:2000, Jackson Immunoresearch). Discs were washed for 20 min in PBS-Triton X-100 0.1%, then
490 mounted in VectaShield mounting medium. For experiments in which H2Av-mRFP was used as the
491 nuclear marker, discs were fixed in 4% (w/v) paraformaldehyde/PBS for ~45 min and goat anti-mouse
492 Pacific Blue antibody (Life Technologies, 1:200 dilution) was used as the secondary antibody.

493 Samples were kept in the dark at -20°C and imaged no later than 18-24 hr after fixation. 1024 x
494 1024 16-bit images were captured using either a Zeiss LSM880 or a Leica SP5 confocal microscope
495 equipped with 40X oil objectives. During imaging, discs were oriented with the equator parallel to the x-
496 axis of the image. Optical slices were set at 0.8µm slices (45-60 optical slices) with an additional digital
497 zoom of 1.2-1.4 to completely image eye discs from basal to apical surfaces. Images recorded a region
498 of at least 6 rows of ommatidia on each side or the dorsal-ventral eye disc equator. All discs for a given
499 condition were fixed, mounted, and imaged in parallel to reduce measurement error. Sample preparation,
500 imaging, and analysis were not performed under blind conditions, nor was sex of the animals noted at
501 time of dissection.

502 **Quantification of expression levels**

503 A minimum of three experimental replicate eye discs were imaged for each experimental
504 condition, with the exception of the *sev>Ras*^{V12} condition for which only one control disc was available.
505 For each imaged wild type eye disc, ~160 R8, ~320 R2/5, ~300 R3/4, ~260 R1/6, ~ 220 R7 and >1000
506 progenitor cells were identified. Empirically, the replicate number of three eye discs provided
507 reproducible composite dynamics. No outlier eye discs were found for any experimental condition, so all
508 samples were included in analysis. The sample size was not pre-computed before data collection.
509 Expression dynamics were inferred from confocal image stacks using an updated version of the
510 segmentation and annotation pipeline described in Peláez et al. 2015. The new pipeline includes
511 *Silhouette,* an open-source package for macOS that integrates our image segmentation algorithm with a
512 GUI (graphical user interface) for cell type annotation. Subsequent analysis and visualization procedures
513 were carried out using the accompanying *FlyEye* python package, which is freely available on GitHub.

514 Cell nuclei segmentation was performed using either H2Av-mRFP (Figures 1, 2, and 4, and their
515 figure supplements) or DAPI (Figures 3 and 5, and their figure supplements) signals as a reference
516 channel to identify individual nuclear boundaries. Nuclei expressing H2Av-mRFP were segmented using
517 the *Silhouette* app's optimized implementation of the GraphCut algorithm (Qi et al 2013), while DAPI-
518 stained discs were segmented using an open-source implementation of the watershed algorithm
519 designed to mitigate the effect of bright spots caused by DAPI accumulation in nucleoli (Bernasek et al.,
520 2020). Each layer of the confocal stack was segmented independently in both cases. A single contour
521 containing each unique cell was manually selected and assigned a cell type (cell state) using *Silhouette*,
522 with care taken to avoid annotating nucleolar contours rather than complete nuclear contours in DAPI-
523 stained discs.

524 For each annotated nucleus contour, expression measurements were obtained by normalizing
525 the mean fluorescence of the Pnt-GFP and Yan antibody channels by the mean fluorescence of the
526 reference channel. This normalization mitigates variability due to potentially uneven sample illumination,
527 segment area, nuclear volume, and in the case of His-RFP, differences in protein expression capacity
528 between cells.

529 **Conversion of distance to time**

530 Cell positions along the anterior-posterior axis were mapped to developmental time as described
531 previously (Peláez et al. 2015). This is predicated on two assumptions: the furrow proceeds at a constant
532 rate of one column of R8 neurons per two hours; and minimal cell migration occurs. For each disc,
533 Delaunay triangulations were used to estimate the median distance between adjacent columns of R8
534 neurons (Fortune and Steven, 1992). We used the median rather than the mean distance because it
535 minimized the influence of non-adjacent R8s that were falsely identified by the triangulation (Peláez et al.
536 2015). Dividing the furrow velocity of 2 h per column by this median distance yields a single conversion
537 factor from position along the anterior-posterior axis to developmental time. This factor was applied to all
538 cell measurements within the corresponding disc, yielding expression time series. Notably, these are not
539 single cell dynamics, but rather aggregate dynamics across the development time course of a cell
540 population.

541 **Computation of moving averages and confidence intervals**

542 Moving averages were computed by first-order Savitzky-Golay filtration (Savitzky and Golay,
543 1964). This method augments the simple windowing approach used in Peláez et al. 2015 by enabling
544 visualization of expression trends at early time-points that are otherwise obscured by large window sizes.
545 A secondary first-order filtration with one-fifth the original window size was applied to smooth lines for
546 visualization purposes.

547 None of our conclusions are sensitive to our choice of filtration or smoothing method (Peláez et
548 al. 2015). Primary window sizes of 250 and 75 cells were used for reporting the expression of multipotent
549 and differentiated cells, unless noted otherwise. Confidence intervals for the moving average were
550 inferred from the 2.5th and 97.5th percentile of ten thousand point estimates of the mean within each
551 window. Point estimates were generated by bootstrap resampling with replacement of the expression
552 levels within each window.

553 **Alignment of expression data**

554 Cells were aligned with a reference population by shifting them in time. The magnitude of this
555 shift was determined by maximizing the cross-correlation of progenitor Pnt-GFP expression *Y(t)* with the
556 corresponding reference time series *X(t)*. Rather than raw measurements, moving averages within a
557 window of ten cells were used to improve robustness against noise. This operation amounts to:

558 $$z = \underset{dt}{\operatorname{argmax}} \ \hat{\gamma}_{X(t),Y(t)}$$

559 $$\hat{\gamma}_{X(t),Y(t)}(dt) = E\Big[\frac{(Y(t+dt)-\mu_Y)(X(t)-\mu_X)}{\sigma_Y \sigma_X}\Big]$$

560 where, μ and σ are the mean and standard deviation of each time series, and *dt* is the time shift by which
561 the population should be shifted.

562 For each experimental treatment, a disc was randomly chosen and shifted in time such that time
563 zero corresponds to the first annotated R8 neuron. This disc then served as the reference population for
564 the alignment of all subsequent biological replicates within the treatment. Similarly, different experimental
565 treatments (e.g. control and perturbation) were aligned by first aligning the discs within each treatment,
566 then aggregating all cells within each treatment and repeating the procedure with the first treatment
567 serving as the reference.

568 This approach differs from the previous implementation of our pipeline in which discs were
569 manually aligned by the inflection point of their Yan-YFP expression profiles. Manual alignment entails
570 arbitrary prioritization of certain dynamic features over others. Our revised protocol yields consistent,
571 reproducible alignment of expression time series that equally weighs the entire time course. The
572 automated approach is more principled but less robust than the manual approach. Specifically, it fails
573 when dynamic forms qualitatively differ between experimental treatments. In these instances, we revert
574 to manual alignment using the inflection point of Pnt-GFP induction as a reference.

575 **Simple competitive binding model**

576 Figure 6 - figure supplement 1 presents results for an equilibrium model of two species, Yan (Y)
577 and Pnt (P), competing for a finite pool of shared binding sites, S:

578 $$Y + S \overset{K_{D,Yan}}{\Longleftrightarrow} SY$$

579 $$P + S \overset{K_{D,Pnt}}{\Longleftrightarrow} SP$$

580 where $K_{D,Yan}$ and $K_{D,Pnt}$ are equilibrium association constants and SY and SP denote the bound species.
581 Applying a mass balance to the total protein and binding site (S_0) abundances:

$$Y_0 = Y + SY$$

$$P_0 = P + SP$$

$$S_0 = S + SY + SP$$

yields an analytically tractable system of nonlinear equations (Wang, 1995). For each pair of absolute protein abundances (Y_0, P_0) in Figure 6 - figure supplement 1B, the Pnt binding site occupancy is simply SP/S_0.

Competitive binding model with cooperativity

The model presented in Figure 6 expands upon the work of Hope, Rebay, and Reinitz (2017). The model is based on a single cis-regulatory element consisting of *n* adjacent binding sites, each of which may be designated as ETS or non-ETS. Each binding site may exist in one of three binding states; bound by a single copy of Yan, bound by a single copy of Pnt, or unbound. Thermodynamic potentials were assigned to each binding state using two parameters for each transcription factor. The parameter α_X defines the free energy of transcription factor *X* binding to an ETS site, while β_X defines the free energy of binding to a non-ETS site (Figure 6 - figure supplement 2A). A unique configuration of binding states for all *n* binding sites constitutes a single microstate, *k*. The thermodynamic potential of each microstate was taken to be the sum of thermodynamic potentials for each of its constituent binding sites. For each microstate, the stabilizing effect of polymerization was incorporated via a third parameter, γ_X, that defines the free energy of SAM-SAM binding between a pair of similar transcription factors bound to adjacent sites. The net result is a total thermodynamic potential, ΔG_k, for each microstate. An example enumeration of all possible microstates for an element consisting of one ETS site preceding two non-ETS sites is provided in Figure 6 - figure supplement 2B. The statistical frequencies of each microstate were evaluated by constructing a canonical ensemble:

$$p_k = \frac{exp(\frac{-\Delta G_k}{RT})[P]^{a_P(k)}[Y]^{a_Y(k)}}{\sum_k exp(\frac{-\Delta G_k}{RT})[P]^{a_P(k)}[Y]^{a_Y(k)}}$$

in which p_k is the statistical frequency of microstate *k*, *[P]* is the Pnt concentration, *[Y]* is the Yan concentration, $a_P(k)$ and $a_Y(k)$ are functions representing the number of bound molecules of *P* and *Y* within microstate k, *T* is a fixed temperature set to 300 K, and *R* is the gas constant. Fractional

occupancies for each binding site correspond to the cumulative statistical frequency of all microstates in which the site is occupied by a given transcription factor. Overall fractional occupancies are similarly evaluated across all sites within the element.

We considered regulatory elements comprised of 12 binding sites in which only the first site carries the ETS designation. We retained the same parameterization of Yan binding proposed by Hope, Rebay, and Reinitz (2017): α_Y=-9.955 kcal mol^{-1}, β_Y=-5.837 kcal mol^{-1}, and γ_Y=-7.043 kcal mol^{-1}. We parameterized Pnt binding thermodynamics to provide balanced competition between Pnt and Yan in the absence of any SAM-mediated polymerization of Pnt. That is, we set Pnt binding affinities such that the transition from Pnt to Yan occupancy occurs when Pnt and Yan concentrations are approximately equal. The model used to generate Figure 6D-F assumes that Pnt binds individual sites with elevated affinities $\alpha_P = 0.96(\alpha_Y + \gamma_Y)$ and $\beta_P = 0.96(\beta_Y + \gamma_Y)$. The model used to generate Figure 6A-C uses these same elevated binding affinities for Yan, while setting γ_Y=0 kcal mol^{-1}. Qualitatively, our results are not sensitive to this parameterization.

Statistical frequencies of all microstates were enumerated using a recursive graph-traversal algorithm implemented in python, where each node in the graph represents an individual binding site and each edge reflects occupancy by a specific transcription factor. An open-source python implementation of this modeling framework has been published on GitHub (https://doi.org/10.5281/zenodo.5520493).

Data and software availability

All segmented and annotated eye discs will be deposited in a data repository upon publication. A series of Jupyter notebooks that use these data to reproduce all analysis, simulations, and figures presented in this manuscript has also been made available (https://github.com/sbernasek/pnt_yan_ratio). The *Silhouette* app used to segment nuclei in eye discs expressing His-RFP and annotate nuclei in all eye discs is freely available via the macOS App Store, while the *FlyEye* python package used to generate, align, and visualize expression dynamics has been published on GitHub (https://doi.org/10.5281/zenodo.5520468).

ACKNOWLEDGEMENTS

We thank Kevin White's lab and the MODEncode Consortium for recombineering the Pnt-GFP transgene, the Howard Hughes Medical Institute (N.P.), the Chicago Biomedical Consortium (N.P), the

Robert Lurie Northwestern Cancer Center (N.P.), the NIH (EY025957, I.R. and R.W.C; GM118144, R.W.C.; GM080372, I.R.), the NSF (1764421, L.A.N.A., N.B. and R.W.C), and Simons Foundation (597491 L.A.N.A., N.B. and R.W.C) for funding, the Bloomington Drosophila Stock Center for flies, Laura Nilson for the use of computational resources, the Developmental Studies Hybridoma Bank for antibody reagents, and the Northwestern Biological Imaging Facility (BIF) for technical imaging support.

REFERENCES

Banerjee U, Renfranz PJ, Hinton DR, Rabin BA, Benzer S. 1987. The sevenless+ protein is expressed apically in cell membranes of developing Drosophila retina; it is not restricted to cell R7. *Cell* **51**:151–158. doi:10.1016/0092-8674(87)90020-1

Basler K, Hafen E. 1989. Dynamics of Drosophila eye development and temporal requirements of sevenless expression. *Development* **107**:723–731.

Bernasek SM, Peláez N, Carthew RW, Bagheri N, Amaral LAN. 2020. Fly-QMA: Automated analysis of mosaic imaginal discs in Drosophila. *Plos Comput Biol* **16**:e1007406. doi:10.1371/journal.pcbi.1007406

Brunner D, Ducker K, Oellers N, Hafen E, Scholz H, Klambt C. 1994. The ETS domain protein pointed-P2 is a target of MAP kinase in the sevenless signal transduction pathway. *Nature* **370**:386–389.

Campos-Ortega JA, Hofbauer A. 1977. Cell clones and pattern formation: On the lineage of photoreceptor cells in the compound eye ofDrosophila. *Wilehm Roux Arch Dev Biol*. doi:10.1007/bf00848423

Edgar BA, Odell GM, Schubiger G. 1989. A genetic switch, based on negative regulation, sharpens stripes in greater embryos. *Dev Genet*. doi:10.1002/dvg.1020100303

Flores GV, Duan H, Yan H, Nagaraj R, Fu W, Zou Y, Noll M, Banerjee U. 2000. Combinatorial signaling in the specification of unique cell fates. *Cell* **103**:75–85.

663 Fortini ME, Simon MA, Rubin GM. 1992. Signalling by the sevenless protein tyrosine kinase is mimicked
664 by Ras1 activation. *Nature* **355**:559–561.

665 Fortune, Steven. 1992. Voronoi Diagrams and Delaunay Triangulations. *Computing in Euclidean*
666 *Geometry*. doi:Fortune, Steven

667 Freeman M. 1996. Reiterative use of the EGF receptor triggers differentiation of all cell types in the
668 Drosophila eye. *Cell* **87**:651–60.

669 Frick CL, Yarka C, Nunns H, Goentoro L. 2017. Sensing relative signal in the Tgf-β/Smad pathway. *Proc*
670 *National Acad Sci* **114**:E2975–E2982. doi:10.1073/pnas.1611428114

671 Gabay L, Scholz H, Golembo M, Klaes A, Shilo BZ, Klambt C. 1996. EGF receptor signaling induces
672 pointed P1 transcription and inactivates Yan protein in the Drosophila embryonic ventral ectoderm.
673 *Development* **122**:3355–62.

674 Gardner TS, Cantor CR, Collins JJ. 2000. Construction of a genetic toggle switch in Escherichia coli.
675 *Nature*. doi:10.1038/35002131

676 Gillespie MA, Palii CG, Sanchez-Taltavull D, Shannon P, Longabaugh WJR, Downes DJ, Sivaraman K,
677 Espinoza HM, Hughes JR, Price ND, Perkins TJ, Ranish JA, Brand M. 2020. Absolute Quantification
678 of Transcription Factors Reveals Principles of Gene Regulation in Erythropoiesis. *Mol Cell* **78**:960-
679 974.e11. doi:10.1016/j.molcel.2020.03.031

680 Goentoro L, Kirschner MW. 2009. Evidence that Fold-Change, and Not Absolute Level, of β-Catenin
681 Dictates Wnt Signaling. *Mol Cell* **36**:872–884. doi:10.1016/j.molcel.2009.11.017

682 Graham TGW, Tabei SMA, Dinner AR, Rebay I. 2010. Modeling bistable cell-fate choices in the
683 Drosophila eye: qualitative and quantitative perspectives. *Development* **137**:2265–2278.
684 doi:10.1242/dev.044826

685 Green SM, Coyne HJ, P. M L, Graves BJ. 2010. DNA Binding by the ETS Protein TEL (ETV6) Is
686 Regulated by Autoinhibition and Self-association. *J Biol Chem* **285**:18496–18504.
687 doi:10.1074/jbc.m109.096958

688 Halfon MS, Carmena A, Gisselbrecht S, Sackerson CM, Jimenez F, Baylies MK, Michelson AM. 2000.
689 Ras pathway specificity is determined by the integration of multiple signal-activated and tissue-
690 restricted transcription factors. *Cell* **103**:63–74.

691 Hope CM, Rebay I, Reinitz J. 2017. DNA Occupancy of Polymerizing Transcription Factors: A Chemical
692 Model of the ETS Family Factor Yan. *Biophys J* **112**:180–192. doi:10.1016/j.bpj.2016.11.901

693 Jacob F, Monod J. 1961. Genetic regulatory mechanisms in the synthesis of proteins. *J Mol Biol*.
694 doi:10.1016/s0022-2836(61)80072-7

695 Jarman AP, Grell EH, Ackerman L, Jan LY, Jan YN. 1994. Atonal is the proneural gene for Drosophila
696 photoreceptors. *Nature* **369**:398–400. doi:10.1038/369398a0

697 Jemc J, Rebay I. 2006. Characterization of the split ends-like gene spenito reveals functional antagonism
698 between SPOC family members during Drosophila eye development. *Genetics* **173**:279–286.

699 Karim FD, Chang HC, Therrien M, Wassarman DA, Laverty T, Rubin GM. 1996. A screen for genes that
700 function downstream of Ras1 during Drosophila eye development. *Genetics* **143**:315–329.

701 Kim CA, Phillips ML, Kim W, Gingery M, Tran HH, Robinson MA, Faham S, Bowie JU. 2001.
702 Polymerization of the SAM domain of TEL in leukemogenesis and transcriptional repression. *Embo J*
703 **20**:4173–82.

704 Kopp JL, Ormsbee BD, Desler M, Rizzino A. 2008. Small Increases in the Level of Sox2 Trigger the
705 Differentiation of Mouse Embryonic Stem Cells. *Stem Cells* **26**:903–911. doi:10.1634/stemcells.2007-
706 0951

707 Lachance JFB, Pelaez N, Cassidy JJ, Webber JL, Rebay I, Carthew RW. 2014. A comparative study of
708 Pointed and Yan expression reveals new complexity to the transcriptional networks downstream of
709 receptor tyrosine kinase signaling. *Dev Biol* **385**:263–278. doi:10.1016/j.ydbio.2013.11.002

710 Lachance J-FB, Webber JL, Hong L, Dinner AR, Rebay I. 2018. Cooperative recruitment of Yan via a
711 high-affinity ETS supersite organizes repression to confer specificity and robustness to cardiac cell
712 fate specification. *Gene Dev* **32**:389–401. doi:10.1101/gad.307132.117

713 Laslo P, Spooner CJ, Warmflash A, Lancki DW, Lee H-J, Sciammas R, Gantner BN, Dinner AR, Singh
714 H. 2006. Multilineage Transcriptional Priming and Determination of Alternate Hematopoietic Cell
715 Fates. *Cell* **126**:755–766. doi:10.1016/j.cell.2006.06.052

716 Li X, Cassidy JJ, Reinke CA, Fischboeck S, Carthew RW. 2009. A microRNA imparts robustness against
717 environmental fluctuation during development. *Cell* **137**:273–282. doi:10.1016/j.cell.2009.01.058

718 Lin Y, Sohn CH, Dalal CK, Cai L, Elowitz MB. 2015. Combinatorial gene regulation by modulation of
719 relative pulse timing. *Nature* **527**:54–58. doi:10.1038/nature15710

720 Lucchesi JC, Rawls JM. 1973. Regulation of gene function: a comparison of enzyme activity levels in
721 relation to gene dosage in diploids and triploids of Drosophila melanogaster. *Biochem Genet* .
722 doi:10.1007/bf00485589

723 Mackereth CD, Scharpf M, Gentile LN, MacIntosh SE, Slupsky CM, P. M L. 2004. Diversity in structure
724 and function of the Ets family PNT domains *J Mol Biol* **342**:1249–1264.

725 Melen GJ, Levy S, Barkai N, Shilo BZ. 2005. Threshold responses to morphogen gradients by zero-order
726 sensitivity. *Molecular Systems Biology* **10**:1–11.

727 Meruelo AD, Bowie JU. 2009. Identifying polymer-forming SAM domains. *Proteins* **74**:1–5.
728 doi:10.1002/prot.22232

729 Nagaraj R, Canon J, Banerjee U. 2002. Cell fate specification in the Drosophila eye. *Results Probl Cell*
730 *Differ* . doi:10.1007/978-3-540-45398-7_6

731 Nitta KR, Jolma A, Yin Y, Morgunova E, Kivioja T, Akhtar J, Hens K, Toivonen J, Deplancke B, Furlong
732 EEM, Taipale J. 2015. Conservation of transcription factor binding specificities across 600 million
733 years of bilateria evolution. *Elife* **4**:e04837. doi:10.7554/elife.04837

734 Niwa H, Miyazaki J, Smith AG. 2000. Quantitative expression of Oct-3/4 defines differentiation,
735 dedifferentiation or self-renewal of ES cells. *Nat Genet* **24**:372–376. doi:10.1038/74199

736 O'Neill EM, Rebay I, Tjian R, Rubin GM. 1994. The activities of two Ets-related transcription factors
737 required for Drosophila eye development are modulated by the Ras/MAPK pathway. *Cell* **78**:137–147.

738 Peláez N, Gavalda-Miralles A, Wang B, Navarro HT, Gudjonson H, Rebay I, Dinner AR, Katsaggelos AK,
739 Amaral LA, Carthew RW. 2015. Dynamics and heterogeneity of a fate determinant during transition
740 towards cell differentiation. *Elife* **4**:e08924. doi:10.7554/elife.08924

741 Qiao F, Song H, Kim CA, Sawaya MR, Hunter JB, Gingery M, Courey AJ, Rebay I, Bowie JU. 2004a.
742 Derepression by Depolymerization: Structural Insights into the Regulation of Yan by Mae. *Cell*
743 **118**:163–173.

744 Qiao F, Song HY, Kim CA, Sawaya MR, Hunter JB, Gingery M, Rebay I, Courey AJ, Bowie JU. 2004b.
745 Derepression by depolymerization: Structural insights into the regulation of Yan by Mae. *Cell*
746 **118**:163–173. doi:10.1016/j.cell.2004.07.010

747 Raabe T. 2000. The sevenless signaling pathway: variations of a common theme. *Biochim Biophys Acta*
748 **1496**:151–63.

749 Ready DF, Hanson TE, Benzer S. 1976. Development of the Drosophila retina, a neurocrystalline lattice.
750 *Dev Biol* **53**:217–240.

751 Rebay I, Rubin GM. 1995. Yan functions as a general inhibitor of differentiation and is negatively
752 regulated by activation of the Ras1/MAPK pathway. *Cell* **81**:857–866.

753 Savitzky Abraham, Golay MJE. 1964. Smoothing and Differentiation of Data by Simplified Least Squares
754 Procedures. *Analytical Chemistry*. doi:doi.org/10.1021/ac60214a047

755 Schröter C, Rué P, Mackenzie JP, Arias AM. 2015. FGF/MAPK signaling sets the switching threshold of
756 a bistable circuit controlling cell fate decisions in embryonic stem cells. *Development* **142**:4205–4216.
757 doi:10.1242/dev.127530

758 Shwartz A, Yogev S, Schejter ED, Shilo BZ. 2013. Sequential activation of ETS proteins provides a
759 sustained transcriptional response to EGFR signaling. *Development* **140**:2746–2754.
760 doi:10.1242/dev.093138

761 Simon MA, Bowtell DD, Dodson GS, Laverty TR, Rubin GM. 1991. Ras1 and a putative guanine
762 nucleotide exchange factor perform crucial steps in signaling by the sevenless protein tyrosine kinase.
763 *Cell* **67**:701–716.

764 Spitz F, Furlong EEM. 2012. Transcription factors: from enhancer binding to developmental control. *Nat*
765 *Rev Genet* **13**:613–626. doi:10.1038/nrg3207

766 Tomlinson A. 1985. The cellular dynamics of pattern formation in the eye of Drosophila. *J Embryol Exp*
767 *Morphol*. doi:89:313-31

768 Tomlinson A, Bowtell DD, Hafen E, Rubin GM. 1987. Localization of the sevenless protein, a putative
769 receptor for positional information, in the eye imaginal disc of Drosophila. *Cell* **51**:143–150.

770 Tootle TL, Lee PS, Rebay I. 2003. CRM1-mediated nuclear export and regulated activity of the Receptor
771 Tyrosine Kinase antagonist YAN require specific interactions with MAE. *Development* **130**:845–857.

772 Vivekanand P, Rebay I. 2006. Intersection of signal transduction pathways and development. *Annu Rev*
773 *Genet* **40**:139–157.

774 Vivekanand P, Tootle TL, Rebay I. 2004. MAE, a dual regulator of the EGFR signaling pathway, is a
775 target of the Ets transcription factors PNT and YAN. *Mech Dev* **121**:1469–1479.

776 Voas MG, Rebay I. 2004. Signal integration during development: insights from the Drosophila eye. *Dev*
777 *Dyn* **229**:162–175. doi:10.1002/dvdy.10449

778 Wang Z-X. 1995. An exact mathematical expression for describing competitive binding of two different
779 ligands to a protein molecule. *Febs Lett* **360**:111–114. doi:10.1016/0014-5793(95)00062-e

780 Webber JL, Zhang J, Cote L, Vivekanand P, Ni X, Zhou J, Negre N, Carthew RW, White KP, Rebay I.
781 2013a. The Relationship between Long-range Chromatin Occupancy and Polymerization of the
782 Drosophila ETS Family Transcriptional Repressor Yan. *Genetics* 633–649.
783 doi:10.1534/genetics.112.146647

784 Webber JL, Zhang J, Massey A, Sanchez-Luege N, Rebay I. 2018. Collaborative repressive action of the
785 antagonistic ETS transcription factors Pointed and Yan fine-tunes gene expression to confer
786 robustness in Drosophila. *Development* **145**:dev165985. doi:10.1242/dev.165985

787 Webber JL, Zhang J, Mitchell-Dick A, Rebay I. 2013b. 3D chromatin interactions organize Yan chromatin
788 occupancy and repression at the even-skipped locus. *Genes Dev* **27**:2293–2298.
789 doi:10.1101/gad.225789.113

790 Wei G, Badis G, Berger MF, Kivioja T, Palin K, Enge M, Bonke M, Jolma A, Varjosalo M, Gehrke AR,
791 Yan J, Talukder S, Turunen M, Taipale M, Stunnenberg HG, Ukkonen E, Hughes TR, Bulyk ML,
792 Taipale J. 2010. Genome-wide analysis of ETS-family DNA-binding in vitro and in vivo. *Embo J*
793 **29**:2147–2160. doi:10.1038/emboj.2010.106

794 Wolff T, Ready DF. 1991. Cell death in normal and rough eye mutants of Drosophila. *Development*
795 **113**:825–839.

796 Wu C, Lachance J-FB, Ludwig MZ, Rebay I. 2020. A context-dependent bifurcation in the Pointed
797 transcriptional effector network contributes specificity and robustness to retinal cell fate acquisition.
798 *Plos Genet* **16**:e1009216. doi:10.1371/journal.pgen.1009216

799 Xu C, Kauffmann RC, Zhang J, Kladny S, Carthew RW. 2000. Overlapping activators and repressors
800 delimit transcriptional response to receptor tyrosine kinase signals in the Drosophila eye. *Cell* **103**:87–
801 97.

802 Yamada T, Okabe M, Hiromi Y. 2003. EDL/MAE regulates EGF-mediated induction by antagonizing Ets
803 transcription factor Pointed. *Development* **130**:4085–4096.

804 Yao G, Lee TJ, Mori S, Nevins JR, You L. 2008. A bistable Rb–E2F switch underlies the restriction point.
805 *Nat Cell Biol* **10**:476–482. doi:10.1038/ncb1711

806 Zhang J, Graham TG, Vivekanand P, Cote L, Cetera M, Rebay I. 2010. Sterile alpha motif domain-
807 mediated self-association plays an essential role in modulating the activity of the Drosophila ETS
808 family transcriptional repressor Yan. *Mol Cell Biol* **30**:1158–1170. doi:10.1128/mcb.01225-09

809 Zhang T, Ranade S, Cai CQ, Clouser C, Pignoni F. 2006. Direct control of neurogenesis by selector
810 factors in the fly eye: regulation of atonal by Ey and So. *Development* **133**:4881–4889.

811 Zhu LJ, Christensen RG, Kazemian M, Hull CJ, Enuameh MS, Basciotta MD, Brasefield JA, Zhu C,
812 Asriyan Y, Lapointe DS, Sinha S, Wolfe SA, Brodsky MH. 2011. FlyFactorSurvey: a database of
813 Drosophila transcription factor binding specificities determined using the bacterial one-hybrid system.
814 *Nucleic Acids Res* **39**:D111–D117. doi:10.1093/nar/gkq858

815